Coupled aero-servo-elastic method for floating offshore wind turbine wake analysis

Lin Yang [a], Kangping Liao[a], Qingwei Ma[b], Abbas Khayyer[c] , Hanbing Sun[a]

[a] College of Shipbuilding Engineering, Harbin Engineering University, Harbin, 150000, China
[b] School of Mathematics, Computer Science and Engineering, City, University of London, UK
[c] Department of Civil and Earth Resources Engineering, Kyoto University, Japan

Abstract

A new coupled aero-servo-elastic method is developed to model unsteady loads and wakes of Floating Offshore Wind Turbines (FOWTs) with elastic blades, in which the actuator curve embedding (ACE) method is for the first time coupled with a nonlinear finite element rotating beam model, rotor speed and collective blade pitch control strategies in a lab code——HEU-FOWT. The method is capable for efficient aero-servo-elastic simulation of FOWT(s) including wakes on relatively coarse Cartesian grids without requiring empirical tip loss corrections. Tests of an isolated blade and a rotating uniform cantilever beam indicate the static deformations, natural frequencies, modal shapes, and centrifugal stiffening effects are well predicted. Validations ~~s~~ of a bottom-fixed NREL 5MW wind turbine show good accuracy for various aero-servo-elastic results in a wide range of wind speed and the rotor thrust and blade tip out-of-plane (Oop) deformation are found significantly underpredicted by 10.5% and 15.0% at rated condition if aerodynamic center offset effects neglected. Aero-servo-elastic wake analyses of a NREL 5MW wind turbine under specified surge motion show the two control strategies (constant power and constant torque mode) significantly reduced the overall far wake deficit by 38.1% and 35.6%, while blade elasticity only reduced the same quantity by 2.7%.

Keywords:

Actuator curve embedding, Coupled aero-servo-elastic, Floating offshore wind turbine, HEU-FOWT

* Corresponding Author

E-mail address: liaokangping@hrbeu.edu.cn. (Kangping Liao)

1.Introduction

Wind energy is one of the most fast-growing renewable and sustainable energy in the past two decades with the total installed capacity from 24GW in 2001 to 743GW in 2020[1]. To further driven down the levelized cost of electricity, the wind turbine rotor is continuously growing in size with diameter increasing from 126m for the well-known NREL-5MW reference wind turbine (RWT) [2]to 240m for the recent IEA-15MW RWT[3]. For these large-scale wind turbines, the blades are usually manufactured using light-weight and flexible composite materials which can be more susceptible to the influence of aeroelasticity. Proper control strategies are usually required in operation for safety and best performances. For example, generator torque control strategy is usually required to regulate rotor speed to maximize power extraction at below-rated conditions and maintain constant rotor speed at above-rated conditions. Blade pitch control strategy (collective blade pitch control[2] or individual blade pitch control[4]) is usually required to save turbine from overload at above-rated conditions. Detailed reviews on wind turbine control strategies are refer to Ha et al. [5] and Meng et al.[6].

With the recent trend of deploying wind turbines from onshore and shallow waters to deep waters, modern variable-speed pitch-regulated FOWTs can experience additional six degree-of-freedoms (DOFs) platform motions (surge, sway and heave for translations, pitch, roll and yaw for rotations), which leads to power fluctuations, increased fatigue loads, cyclic blade deformations, dynamic rotor speeds and varying blade pitch angles. The coupled aero-servo-elastic nature of flexible blades and floating motions complicate the FOWT wake characteristics, which can be a significant concern for wind energy industrial as the average power losses due to wake interactions can be 10%~20% of the total power for large offshore wind farms according to Barthelmie et al. [7]. Therefore, it is important to take the aerodynamics, structure dynamics and control effects all into consideration to design a compact floating offshore wind farm. For that purpose, an aero-servo-elastic method with acceptable accuracy and affordable efficiency is required.

For structure modeling, a flexible slender structure can be directly modeled as 3D finite elements (solids or shells) or be simplified as 1D beam structure. The 3D solid or shell finite

element model has the potential to provide the most accurate and detailed results for structural dynamics, but it is computationally expensive as shown in Bazilevs et al. [8, 9]and the accuracy improvements for overall responses are limited when compared with nonlinear beam model as shown in Júnior et al [10]. Thus, the beam model, which includes Euler-Bernoulli beam theory, Timoshenko beam theory and Geometrically Exact Beam Theory (GEBT), is preferred for blade aeroelasticity analysis unless the local stress or buckling phenomena is concerned.

The beam structure can be discretized using modal approach, multi-body dynamic (MBD) method and 1D finite element method (FEM). The modal approach represents the blade deformations as a linear combination of precomputed modal shapes, which significantly reduces the modeling DOFs. Although highly efficient, the accuracy of modal approach greatly depends on the number of modes considered and the important torsional DOF was usually neglected. For example, only three bending modes, two modes for flap and one for edge, are used in FAST ElastoDyn [2]. The MBD discretizes the flexible blade into a set of beam elements which are constrained by force or motion relationships[11]. In 1D FEM, the blade is discretized into a series of finite beam elements with shared nodal displacements and can be more accurate than modal or MBD method with slightly increased computational cost [12], so that it is adopted in this paper.

For aerodynamics, many existing aero-servo-elastic analysis tools , such as FAST[2], HAWC2[13] and DARwind[14], are mostly based on the Blade Element Momentum (BEM) method which combines the 1D momentum theory and blade element theory. It is highly efficient and accurate as long as the basic assumptions are valid and many semi-empirical models are well implemented, such as tip/hub loss corrections, dynamic inflow models, stall delay corrections, skewed-wake corrections and dynamic stall models. However, when a FOWT pitches or surges backward at a velocity similar with its ambient wakes, the rotor can operate in a so-called vortex ring state (VSR), a phenomena firstly observed for helicopters in descending flight [15]. In VRS, the tip and root vortices recirculate around the rotor and the basic momentum balance assumption breaks down, then the validity of BEM can be questionable as pointed out by Sebastian et al.[16]. In addition, the BEM-based aero-servo-elastic tools can not directly model turbine wakes unless coupled with other flow solvers.

In recent decade, many endeavors were devoted to coupling high-fidelity geometry-resolving

CFD method with Computational Structural Dynamic (CSD) method for wind turbine aeroelasticity modeling, often referred as CFD-CSD or Fluid Structure Interaction (FSI) approach, wherein the aerodynamic loads are obtained by numerically solving the discretized Navier-Stokes equations with body-fitted meshes and the blade deformations are calculated based on efficient nonlinear beam theories. Additional mesh motion solver should be solved to handle volume mesh displacements. For examples, Yu et al.[17] coupled an in-house CFD code with a structural model based on non-linear flap-lag-torsion beam theory using the delta-airload loose-coupling strategy[18]. Coupled CFD-MBD approaches were proposed by Li et al. [19] Liu et al. [20] Guma et al. [21]. Heinz et al. [22]and Grinderslev et al. [23] coupled blade-resolving CFD code EllipSys3D with existed aero-elastic code HAWC2, and Dose et al.[24] implemented an inhouse structural code BeamFOAM in OpenFOAM. Although the CFD approach provides outstanding forecasts for wind turbine aerodynamic performance, wake flow, and vortex shedding, which cannot be achieved by other BEM-based codes as shown in the works of Alkhabbaz et al. [25, 26]. Regrettably, it demands significant resources in terms of cost, time, and high-performance computing. As reported in Dose et al.[24], it takes approximately 1666 core*hours per rotor revolution using partitioned loose-coupling strategy with 36.38 million cells and parallelized with 360 cores.

Alternative to the low fidelity BEM method and high fidelity CFD-CSD method, the medium fidelity Actuator Line Method (ALM) [27] is a good trade-off between accuracy and efficiency for blade aerodynamics. In ALM, a blade is modelled as an actuator line with distributed aerodynamic forces which are projected to fluid domain as source terms in the discretized Navier-Stokes equations to model the effects of rotating blades on flow. ALM facilitates the usage of relatively coarse Cartesian grids with significantly reduced computational cost comparing with geometry-resolving method while the important wake features such as helical tip/root vortices are well captured, and can be directly extended for turbine-turbine interaction simulations without any theoretical limitations. Coupling the ALM with beam theory based structure model leads to the concept of Elastic Actuator Line Method (EALM), which has been used for evaluating wake effects on fatigue loads for wind farms[28, 29], investigating aeroelastic wake behaviors[30-32], turbine-turbine wake interaction analysis[33, 34] and aero-elastic-hydro-mooring-wake

115 analysis[35].

116 However, several limitations exist for previous works in terms of EALM and some challenges
117 should be well-treated. Many works were focused on bottom-fixed wind turbines with constant
118 rotor speeds and blade pitch angles, which is not fully reflecting the real applications of FOWTs.
119 Comprehensive validations of EALM models in terms of rotor performances and blade
120 deformations in a wide range of wind speeds with satisfactory results are currently absent. Details
121 required for accurate prediction of blade in-plane and torsional deformations which are closely
122 related to the bend-bend coupling and aerodynamic center offset were less discussed. A major
123 challenge for an EALM model is to design a suitable coupling strategy to communicate data
124 between different sub models efficiently while avoiding numerical instabilities.

125 In this paper, a new coupled aero-servo-elastic method for floating offshore wind turbine wake
126 simulation is presented based on the in-house code HEU-FOWT[36]. The previous version of
127 HEU-FOWT can perform aero-servo analysis of FOWTs via an advanced actuator line method
128 with actuator curve embedding (ACE) concept[37] for rigid blade aerodynamics and including
129 generator torque and full-span, rotor-collective blade pitch control strategies. We extend the
130 capabilities of HEU-FOWT to model blade elasticities using a nonlinear finite element rotating
131 beam theory for structural dynamics. Partitioned loose-coupling strategy is adopted for data
132 communication. For simplicity, only specified platform surge motion is considered. To the best
133 knowledge of the authors, this is the first work endeavored to couple ACE method with a
134 structural model and a control model, and the advantage of this new method is its capability for
135 efficient aero-servo-elastic simulations of FOWT(s) including wakes on coarse Cartesian grids
136 without requiring empirical tip loss corrections.

137 The rest of this paper is organized as follows: in **section 2**, the turbine geometries and
138 numerical methods for the proposed coupled aero-servo-elastic framework are described. The
139 computational domain layouts, mesh discretization and verifications are presented in **Section 3**. In
140 **section 4**, the proposed method is carefully validated and then applied for aero-servo-elastic
141 analysis of a NREL 5MW wind turbine under specified platform surge motions including wake
142 features. The conclusions are summarized in **section 5.**
143

2. Theories and models

2.1 Wind turbine geometry model

The NREL 5MW wind turbine is adopted for simulation. It is a three-bladed variable-speed pitch-regulated horizontal axis wind turbine with diameter $D = 126$ m and hub height $H = 90$ m. Major properties are summarized in **Table 1**. The blade aerodynamic properties are defined by 17 sections and 7 airfoils while the blade structural properties are given on 49 sections. Detailed airfoil aerodynamic coefficient tables and sectional material properties like mass, stiffness and inertial are publicly available in Jonkman et al.[2]. In this paper, only the blade aeroelasticity is considered by modeling the blades as rotating cantilever beams. The influences of hub, nacelle, tower on wake characteristics and the tower flexibility on blade structural responses are currently neglected, but the variations of rotor speeds and blade pitch angles under platform surge motions are considered. The NREL 5MW wind turbine with a OC4 submersible platform is shown in **Fig. 1 (a)** for demonstration, although the wave dynamics are currently neglected.

Table 1 NREL 5MW turbine parameters.

Parameters	values
Diameter (D)	126 m
Number of blades(N_b)	3
Rotor tilt angle	5.0°
Blade upwind precone angle	2.5°
Averaged blade chord ($\bar{c}$)	3.487 m
Cut-in, rated and cut-out wind speed	4m/s, 11.4m/s, 25m/s
Rated rotor speed (Ω_0)	12.1 rpm
Overhang, Hub height	5m, 90m
Blade airfoils	Cylinder1, Cylinder2, DU40,35, 30,25,21 and NACA64

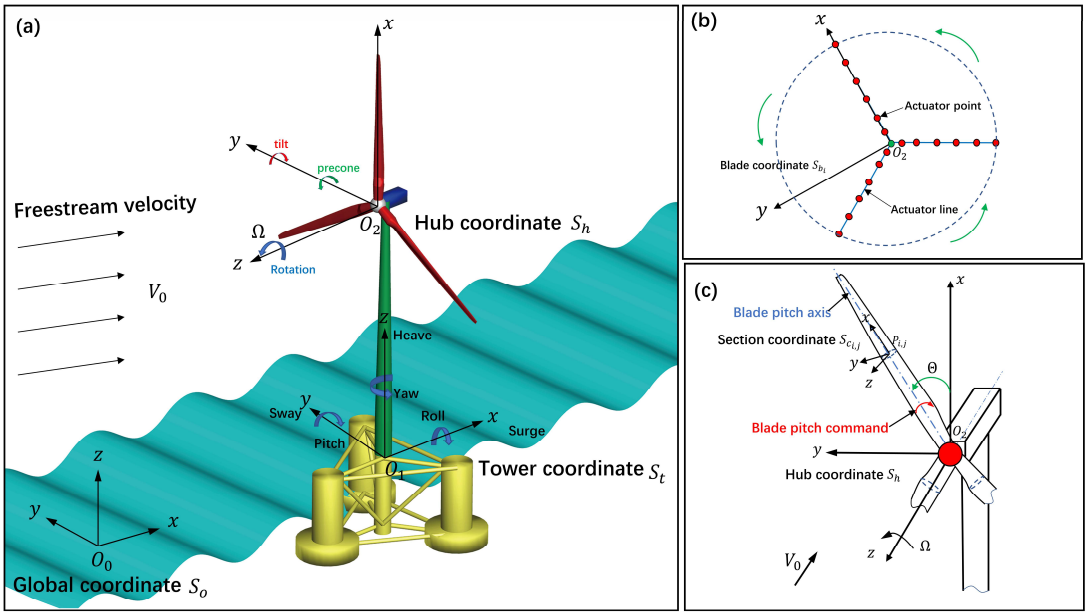

Fig. 1. Floating offshore wind turbine system geometries and kinematics description using different reference coordinate systems.

2.2 Aerodynamic model

2.2.1 Flow solver

In HEU-FOWT, flow field simulation is based on Large Eddy Simulation (LES) wherein large scales are directly resolved using the spatially filtered unsteady incompressible Navier-Stokes equations and small scales are modeled as follows

$$\frac{\partial \bar{u}_i}{\partial x_i} = 0 \tag{1}$$

$$\frac{\partial \bar{u}_i}{\partial t} + \frac{\partial \bar{u}_i \bar{u}_j}{\partial x_j} = -\frac{1}{\rho_a}\frac{\partial \bar{P}}{\partial x_i} + \nu \frac{\partial^2 \bar{u}_i}{\partial x_j \partial x_j} - \frac{\partial \tau_{ij}}{\partial x_j} + \frac{1}{\rho_a} F_i \tag{2}$$

where $\bar{u}_i$ donate the filtered velocity vectors with $i = 1,2,3$ corresponding to the x, y and z directions in the global inertial coordinate system S_0 (**Fig. 1 (a)**). ν is kinematic viscosity. ρ_a is air density. $\tau_{ij} = \overline{u_i u_j} - \bar{u}_i \bar{u}_j = -2\nu_t \bar{S}_{ij}$ is the sub-grid scale (SGS) stress tensor modeling the effects of small scales. $S_{ij} = \frac{1}{2}\left(\frac{\partial \bar{u}_i}{\partial x_j} + \frac{\partial \bar{u}_j}{\partial x_i}\right)$ is the symmetric part of the resolved velocity gradient tensor. ν_t is the sub-grid scale viscosity modeled by standard Smagorinsky SGS model as $\nu_t = (C_s \Delta)^2 |\bar{S}_{ij}|$ with $C_s = 0.15$ is the Smagorinsky coefficient and $\Delta = \left(\Delta_x \Delta_y \Delta_z\right)^{1/3}$ is the filter width. Δ_x,Δ_y and Δ_z are grid resolutions in x, y and z directions in global inertial coordinate

system. The effects of rotating blades on fluid flow are modelled as the body force term F_i which is detailed in **Section 2.2.2**, thus LES can be used on relatively coarse Cartesian grids as direct resolving of small-scale turbulences in near wall (blade surfaces) region is avoided.

Eqs. (1) and **(2)** are numerically solved on staggered stretching Cartesian grids using fractional projection method with Constrained Interpolation Profile (CIP) method [38] including one predictor step and two corrector steps. The CIP method, which consists of an advection step and a non-advection step, is used for the predictor step and the first corrector step. In the advection step, an intermediate velocity field is predicted by solving the advection equation $\frac{\partial \bar{u}_i}{\partial t} + \bar{u}_j \frac{\partial \bar{u}_i}{\partial x_j} = 0$ using a semi-Lagrange approach which has low numerical diffusion and sub cell resolution with compact upwind scheme. Then, the velocity field is corrected by viscous and body force term in the non-advection step. A pressure Poisson equation is solved to update pressure field and the velocity field is corrected again by the new pressure field. More details on the implementation of CIP can refer to the work Hu and Kashiwagi[39]. The pressure gradient term and viscous term are spatially discretized by central difference scheme.

2.2.2 Actuator curve embedding model

The advanced actuator line method with actuator curve embedding concept (donated as Actuator Curve Embedding method in this paper) proposed by Jha and Schmitz[37] is utilized to construct the body force term F_i on the right-hand side of **Eq. (2)**. **Fig. 1(b)** shows the actuator line representation of wind turbine blades with discrete actuator points. For the j^{th} section of i^{th} blade, the section aerodynamics are calculated in the local section coordinate system $S_{c_{i,j}}$ using quasi-steady 2D theory as in **Fig. 2**.

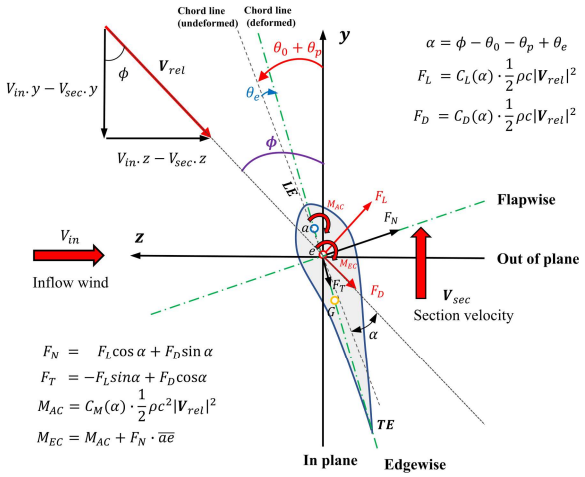

Fig. 2. Blade sectional aerodynamics. a is aerodynamic center and e is the pitch axis positoin.

Firstly, the relative velocity between each blade section and flow at sectional aerodynamic center (AC) is calculated as

$$\boldsymbol{V}_{rel} = \boldsymbol{V}_{in} - \boldsymbol{V}_{rot} - \boldsymbol{V}_{platform} - \boldsymbol{V}_{elastic} \tag{3}$$

where $\boldsymbol{V}_{in}$ is the flow velocity sampled at AC point; $\boldsymbol{V}_{rot}$, $\boldsymbol{V}_{platform}$ and $\boldsymbol{V}_{elastic}$ is the velocity at AC due to rotor rotation, platform floating motions and blade elastic deformations, respectively. The velocities induced by blade pitch command and blade elastic torsional deformations are currently neglected in **Eq. (3)**.

Then, the local angle of attack is obtained as

$$\alpha = \phi - \theta_0 - \theta_p + \theta_e \tag{4}$$

where $\phi = \tan^{-1}\left(\frac{-V_{rel,z}}{-V_{rel,y}}\right)$ is the local velocity inflow angle; θ_0, θ_p and θ_e is the initial twist angle, blade pitch angle and elastic torsional angle for each blade section, respectively. Positive θ_e indicates nose-up direction which points to the negative x direction in section coordinate system $S_{c_{i,j}}$.

Finally, the sectional aerodynamic loads are calculated as

$$F_L = C_L(\alpha)\frac{1}{2}\rho c|\boldsymbol{V_{rel}}|^2 \tag{5}$$

$$F_D = C_D(\alpha)\frac{1}{2}\rho c|\boldsymbol{V_{rel}}|^2 \tag{6}$$

$$M_{AC} = \frac{1}{2}C_M(\alpha)\rho c^2|\boldsymbol{V_{rel}}|^2 \tag{7}$$

$$M_{PA} = \frac{1}{2}C_M(\alpha)\rho c^2|\boldsymbol{V_{rel}}|^2 + F_n * \overline{ae} \tag{8}$$

where c is local chord; C_L, C_D and C_M are sectional lift, drag and moment coefficients which are

interpolated from respective airfoil table according to local angle of attack α; F_L and F_D are sectional lift and drag forces; M_{AC} and M_{PA} are sectional aerodynamic moments against the aerodynamic center and pitch axis position, respectively. $\overline{ae}$ is the chordwise distance between aerodynamic center (a) and pitch axis (e). $F_N = F_L\cos(\alpha) + F_D\sin(\alpha)$ and $F_T = -F_L\sin(\alpha) + F_D\cos(\alpha)$ are normal and tangential forces relative to local chord line.

The aerodynamic coefficients C_L, C_D and C_M in the airfoil tables are defined on sectional aerodynamic centers and the blade pitch axis is defined as the reference line in structural model.. Therefore, the aerodynamic moments used for aeroelastic simulations should be calculated using **Eq. (8)** instead of **Eq. (7)** to account for the AC offset effects which have been neglected by many previous works [30] [40] [41] [42], although it has been well addressed in the many BEM-based codes, such as FAST, and some vortex lattice code[43]. The positions of blade pitch axis and aerodynamic centers are schematically shown in **Fig. 3** following the more physically consistent definitions in the post of [44] instead of the original one[2], but the relative chordwise distance between pitch axis and AC is identical at each section for the two definitions which will not bring different results for lifting line based methods, such as BEM and ACE.

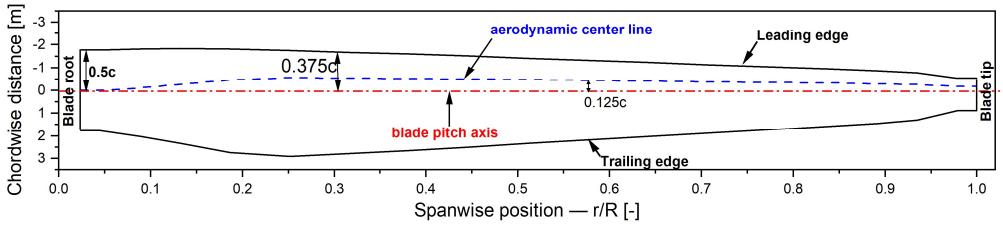

Fig. 3. Schematic of the NREL 5MW wind turbine blade with pitch axis and aerodynamic center line.

ACE differs from ALM only in the force projection process (See **Fig. 4**). In ALM, the body force term F_i at a grid point in fluid domain is obtained by accumulating the projected aerodynamic forces (using 3D Gaussian kernels) of all blade segments of al blades. This treatment leads to force overlapping and projecting body force beyond blade tips, so that the blade loads are usually overpredicted in tip regions and empirical tip loss corrections are always required for remedy. In ACE concept, the blade forces are only projected in the plane normal to the actuator curve. For a grid in fluid domain (see Q_0 in **Fig. 4**) to be influenced by blade forces, it is first associated with an artificial section between two actuator points P_m and P_{m+1} of each actuator curve (see the point F in **Fig. 4**), where point F is determined by keeping $\overline{Q_0F}$ normal to the

actuator curve. The blade forces at the artificial section are interpolated using neighboring information and then are project to grid point Q_0 using 2D Gaussian kernels. Looping over the N_b blades, the body force experienced by grid Q_0 can be expressed as

$$F_i = -\sum_{k=1}^{N_b} f_{k,i}^* \left[\frac{1}{\pi \varepsilon^{*2}} e^{-\left(\frac{r_n}{\varepsilon^*}\right)^2} \right] \tag{9}$$

where N_b is the blade number, ε^* is the smooth length scale of the 2D Gaussian kernel at the artificial section, r_n is the normal distance from the grid to the associated blade section. $f_{k,i}^*$ is the i^{th} component of the total aerodynamic force (vector sum of lift and drag in global inertial coordinate system) at the artificial section of k^{th} blade. Both $f_{k,i}^*$ and ε^* are linearly interpolated using neighboring values as

$$f_{k,i}^* = \left(1 - \frac{r_s}{\Delta b_m}\right) f_{k,m,i} + \frac{r_s}{\Delta b_m} f_{k,m+1,i} \tag{10}$$

$$\varepsilon^* = \left(1 - \frac{r_s}{\Delta b_m}\right) \varepsilon_m + \frac{r_s}{\Delta b_m} \varepsilon_{m+1} \tag{11}$$

where Δb_m is the distance between neighboring points P_m and P_{m+1}, r_s is the tangential distance from point P_m along actuator line.ε_m and ε_{m+1} are smooth length scales at points P_m and P_{m+1}. $f_{k,m,i}$ and $f_{k,m+1,i}$ are i^{th} component of total aerodynamic forces at actuator points P_m and P_{m+1} of the k^{th} blade. For a curved actuator line, some fluid points on the concave and convex sides of the actuator curve may need special treatments to obtain the tangential and normal coordinates, which is addressed in Appendix A.

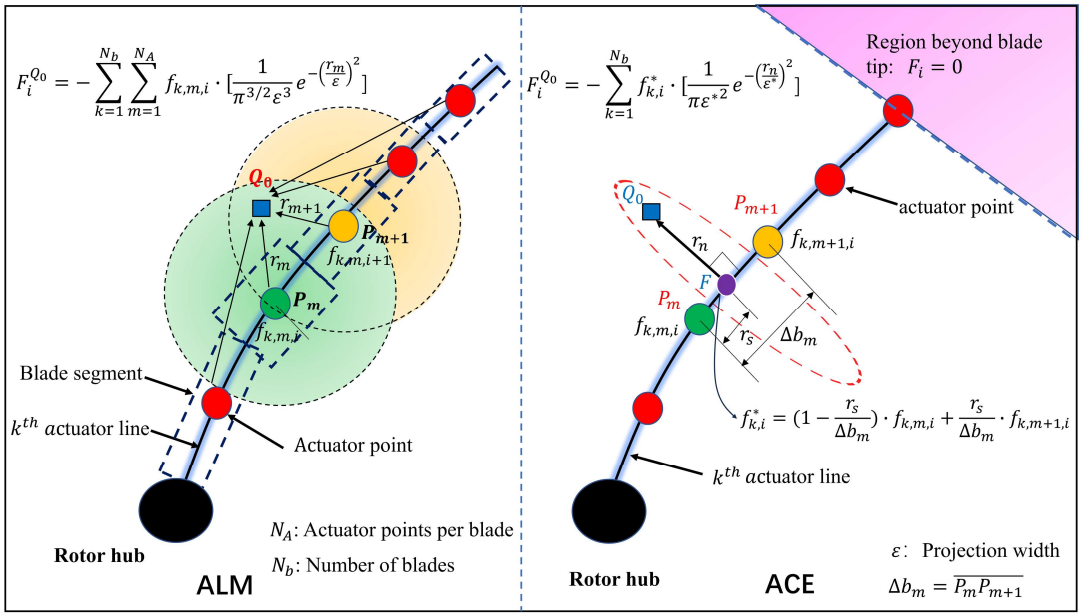

Fig. 4. Comparation of conventional Actuator Line Method (ALM)[27] and Actuator Curve Embedding (ACE)[37] approach in body blade force projection process. Q_0 is an arbitrary grid point in fluid domain.

The 2D Gaussian smooth length scale ε is proportional to the local chord (c^*) of an equivalent elliptic wing of a real blade to approximate the primary mode of blade distributed load. The root chord (c_0) and local chord (c^*) distribution of the equivalent elliptic wing are given in **Eq. (12)** and **(13)**. More details on the ACE implementation and the equivalent elliptic wing approximation can be found in Jha et al.[45]. In this paper, the 2D Gaussian smooth length scale is set as $\varepsilon = 1.2c^*$ based on our previous work Yang et al.[36] and the work of Jha and Schmitz[37].

$$c_0 = \frac{4}{\pi R}\int_0^R c(r)dr = \frac{4\bar{c}}{\pi} \tag{12}$$

$$c^*(r) = c_0\sqrt{1-\left(\frac{2r}{R}-1\right)^2} \tag{13}$$

where R is blade radius and $\bar{c} = \frac{1}{R}\int_0^R c(r)dr$ is the averaged chord length of a real blade.

2.3 Structural model

The blade elasticity modeling is mainly referred to the work of Ma et al.[30], in which the turbine blades are modeled as nonlinear rotating Euler-Bernoulli beams and the beam structures are further discretized by two-node, 12 degrees of freedom (DOF) finite elements (**Fig. 5**). Blade element elastic deformations, including elongation (u_x), torsion (θ_x) and bending deformations (u_y, u_z), are represented using nodal displacements and elemental shape functions as in **Eq. (14)** or in matrix format as **Eq. (16)**. $\boldsymbol{q^e}$ is the element nodal displacement. L is the length of beam element. $\boldsymbol{N_0}$, $\boldsymbol{N_1}$, $\boldsymbol{N_2}$, $\boldsymbol{N_3}$ and $\boldsymbol{N_4}$ are strain matrices.

$$\begin{bmatrix} u_x \\ u_y \\ u_z \\ \theta_x \end{bmatrix} = \begin{bmatrix} \eta_1(x) & 0 & 0 & 0 & 0 & 0 & \eta_2(x) & 0 & 0 & 0 & 0 & 0 \\ 0 & \eta_3(x) & 0 & 0 & 0 & \eta_4(x) & 0 & \eta_5(x) & 0 & 0 & 0 & \eta_6(x) \\ 0 & 0 & \eta_3(x) & 0 & -\eta_4(x) & 0 & 0 & 0 & \eta_5(x) & 0 & -\eta_6(x) & 0 \\ 0 & 0 & 0 & \eta_1(x) & 0 & 0 & 0 & 0 & 0 & \eta_2(x) & 0 & 0 \end{bmatrix} q^e \tag{14}$$

$$\eta_1(x) = 1-\xi, \eta_2(x) = \xi, \eta_3(x) = 1-3\xi^2+2\xi^3, \eta_4(x) = L\xi(1-2\xi+\xi^2)$$

$$\eta_5(x) = 3\xi^2-2\xi^3, \eta_6(x) = L\xi^2(\xi-1), \xi = \frac{x}{L}$$

$$\boldsymbol{q^e} = \begin{bmatrix} u_x^{(1)} & u_y^{(1)} & u_z^{(1)} & \theta_x^{(1)} & \theta_y^{(1)} & \theta_z^{(1)} & u_x^{(2)} & u_y^{(2)} & u_z^{(2)} & \theta_x^{(2)} & \theta_y^{(2)} & \theta_z^{(2)} \end{bmatrix}^T \tag{15}$$

$$\begin{bmatrix} u_x \\ u_y \\ u_z \\ \theta_x \end{bmatrix} = \begin{bmatrix} \boldsymbol{N_1} \\ \boldsymbol{N_2} \\ \boldsymbol{N_3} \\ \boldsymbol{N_4} \end{bmatrix} \boldsymbol{q^e} = \begin{bmatrix} \boldsymbol{N_0} \\ \boldsymbol{N_4} \end{bmatrix} \boldsymbol{q^e} \tag{16}$$

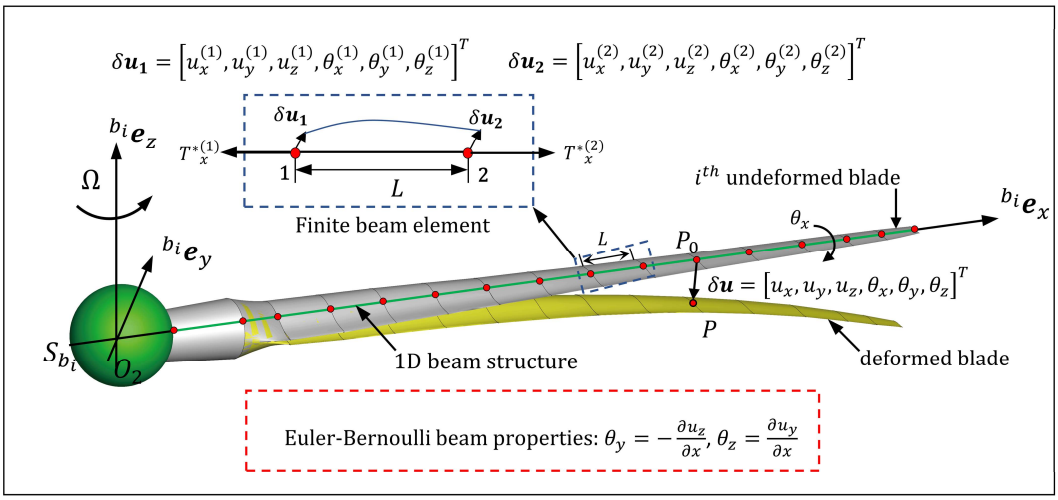

Fig. 5. Schematic of blade elastic deformations and finite beam element representation.

The blade elastic responses are obtained by solving the following discretized equations of motion for each rotating blade using Newmark method,

$$\boldsymbol{M_E}\ddot{\boldsymbol{q}} + \boldsymbol{C_E}\dot{\boldsymbol{q}} + \boldsymbol{K_E}\boldsymbol{q} = \boldsymbol{F_E} \tag{17}$$

where $\boldsymbol{M_E}, \boldsymbol{C_E}, \boldsymbol{K_E}$ are global mass, damping and stiffness matrix, and $\boldsymbol{F_E}$ is the generalized loads for each blade, which are obtained by assembling the blade elemental matrices and r.h.s. By solving the eigen value problem of **Eq. (17)**, the eigen values correspond to the circular natural frequencies and the normalized eigen vectors are modal shapes for each blade. The derivation of elemental matrices and r.h.s are detailed in **Appendix B.**

2.4 Control strategies

The control strategies in the current code are based on the work of Jonkman et al.[2] which consist of a generator torque controller and a full-span rotor-collective blade pitch controller. A low-pass filter is applied to the real-time rotor speed Ω to mitigate high frequency excitation with the filtered rotor speed $\widetilde{\Omega}$ in discrete formulation as

$$\widetilde{\Omega}_{n+1} = (1-\beta)\widetilde{\Omega}_n + \beta\Omega_{n+1} \tag{18}$$

where $\beta = e^{-2\pi f_c \delta t}$ and f_c is corner frequency. δt is timestep size.

The dynamic rotor speed is determined through a single DOF equation with rotor aerodynamic torque (T_a) (against rotor shaft) and generator torque (T_{Gen}) as

$$I_D\dot{\Omega} = T_a - T_{Gen} \tag{19}$$

where I_D is the total drivetrain inertial cast to the low-speed shaft. The real-time generator speed (Ω_{gen}) and filtered generator speed ($\widetilde{\Omega}_{Gen}$) is proportional to real-time rotor speed and filtered rotor speed with gear box ratio (N_{Gear}), respectively. Namely, $\Omega_{Gen} = N_{Gear}\Omega$ and $\widetilde{\Omega}_{Gen} = N_{Gear}\widetilde{\Omega}$.

The generator torque T_{Gen} is calculated as a tabulated function of the filtered generator speed $\widetilde{\Omega}_{Gen}$ according to five defined torque control regions: 1,1$_{1/2}$,2,2$_{1/2}$ and 3 (see **Fig. 6**). In region 1, the generator torque is set to zero as the effective wind speed is lower than cut-in wind speed. In region 2, the generator torque is proportional to the square of the filtered generator speed in order to maximize power extraction by maintaining a constant optimal tip speed ratio. In region 3, the effective wind speed exceeds the rated one and the pitch controller begins to work. The generator torque can be inversely proportional to the filtered rotor speed to maintain a constant generator power (constant power mode) or be maintained as constant nominal torque (constant torque mode). Region 1$_{1/2}$ and 2$_{1/2}$ are two linear transition regions. The output generator power is calculated as $P_{Gen} = \eta T_{Gen}\Omega_{Gen}$ where η is electrical efficiency of generator while the rotor aerodynamic power is calculated as $P_{aero} = T_a\Omega$.

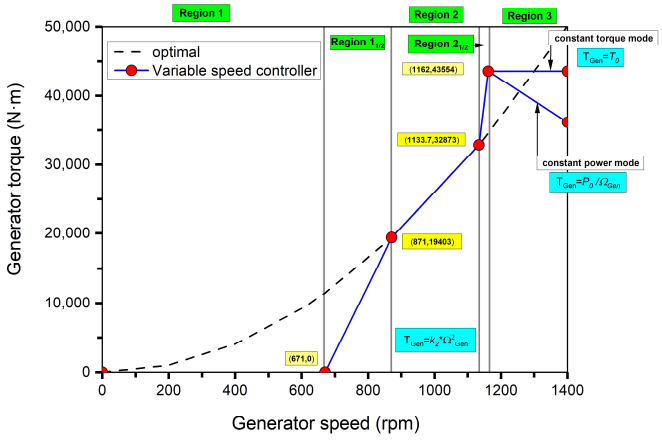

Fig. 6. Generator torque-speed plot.

Based on gain-scheduled proportional-integral (PI) control, the blade pitch command θ_p has the general form of

$$\theta_p = \left(K_{P0} \Delta\Omega + K_{I0} \int_0^t \Delta\Omega dt \right) GK(\theta) N_{Gear} \quad (20)$$

where K_{P0} and K_{I0} is the proportional and integral gains at zero pitch angles. $GK(\theta_p) = \frac{1}{1+\theta_p/\theta_k}$ is a correction factor to account for the variations of proportional and integral gains at non-zero pitch angles. θ_k is the blade pitch angle where the power sensitivity $\frac{\partial P}{\partial \theta_p}$ is doubled compared with rated conditions with zero pitch angle, namely: $\frac{\partial P}{\partial \theta_p}(\theta = \theta_k) = 2\frac{\partial P}{\partial \theta_p}(\theta_p = 0)$. $\Delta\Omega = \Omega - \Omega_0$ is rotor speed error. More details are provide in Jonkman et al. [2] and key parameters are summarized in **Table 2**.

Table 2 Parameters of the NREL 5MW wind turbine controller.

Parameters	Symbols	Values
Rated generator torque	T_0	43,093.55 N•m
Rated generator mechanical power	P_0	5.296610 MW
Electrical efficiency of generator	η	94.4%
Rated generator output power		5.0 MW
Gear box ratio	N_{Gear}	97:1
Generator Torque Constant in Region 2		0.0255764 N•m/rpm^2
Corner frequency for low pass filter	f_c	0.25 Hz
Rated rotor speed	Ω_0	12.1 rpm
Default Proportional Gain at rated point	K_{P0}	0.01882681
Default Integral Gain at rated point	K_{I0}	0.008068634
Pitch Angle with doubled power sensitivity	θ_k	6.30°
Total drivetrain inertial cast to LSS	I_D	43784725.44 kg · m^4

2.5 Aero-servo-elastic coupling strategy

The HEU-FOWT code is written in modern Fortran language with object-oriented programing and can be divided as four major modules: basic CFD solver, ACE module, control module and FEM module. The partitioned loose-coupling strategy is adopted for data communication between different modules while preserving code modularity and avoiding inner loop sub iterations between different sub problems. For each blade, the aerodynamic loads, blade elastic deformations and elastic velocities are communicated between ACE and FEM modules using cubic interpolations. The control module only receives rotor aerodynamic torque as input and output rotor speeds and collective blade pitch angles. Numerical stability of the coupling strategy is

maintained by introducing structural damping term as described in Appendix C. A flow chart describing the coupling procedures is shown in **Fig. 7**.

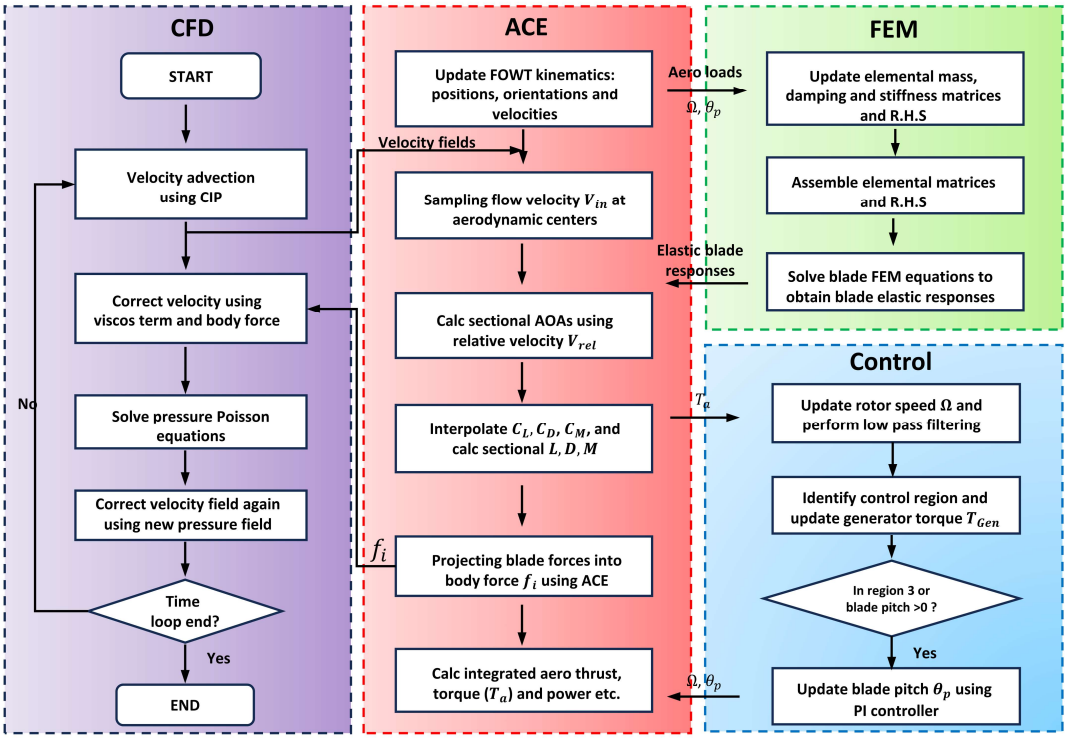

Fig. 7 Flow chart of the current aero-servo-elastic model with partitioned loose-coupling strategy.

3. Computational domain and mesh

The computational domain is $6D$ in width, $H + 3D$ in height, $10D$ in length with the outlet at $7D$ downstream. The domain is discretized by stretching Cartesian grids with a wake refinement region extending $5D$ downstream with finest grid resolution of 2m (approximately 32 grids per blade radius), which is donated as **Grid #1** with a total grid number of 7.3 million ($400 \times 149 \times 122$) as shown in **Fig. 8** . However, if only the rotor loads or blade elastic deformations are concerned, the grid with a smaller wake refinement region extending only $1D$ downstream, which is donated as **Grid #2** with a total grid number of 3.2 million ($178 \times 149 \times 122$), is used to reduce computational time as between using **Grid #1** and **Grid #2** are negligible (simulation results not shown in this paper). In this paper, **Grid #1** is used for surge motion cases and **Grid #2** is used for verifications and validations. A mesh independence test is performed for a bottom-fixed NREL 5MW wind turbine with elastic blades without control (V_0=11.4m/s, Ω=12.1 rpm, $\theta_p = 0°$)

with the time averaged aeroelastic results (over rev. 22-24) are shown in Table 3. As shown, the relative errors between the grid resolutions of 2m and 1.5m are well below 1% for thrust, power, blade tip in-plane and out-of-plane deformations. The large relative error for blade torsion deformation is due to the very small absolute values, which should not introduce too much numerical errors. Therefore, the grid resolution of 2m in wake refinement region is used throughout this paper.

The time step size is determined by restricting the blade to rotate 1° per step and all cases are currently simulated in serial mode without parallelization. The real computational time for each time step is approximately 25.3s for Grid #2 (3.2 M) and 58.6 s for Grid #1 (7.3 M), wherein the computational time introduced by the aero-elastic model is approximately 1.0s for both grids.

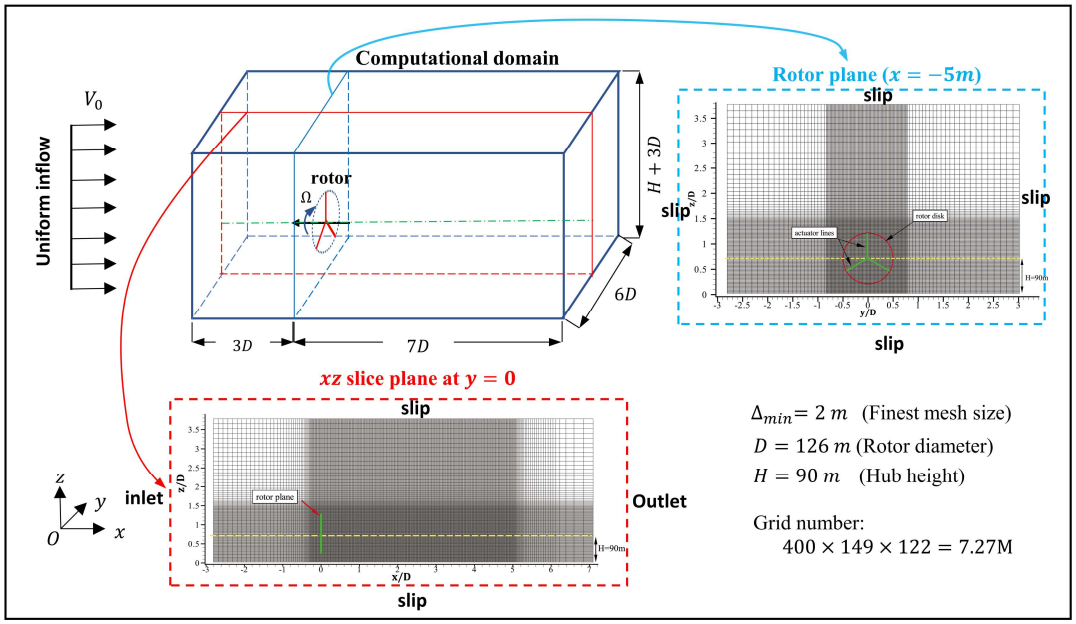

Fig. 8 . Computational domain, boundary conditions and mesh discretization (**Grid #1**).

Table 3 Time-averaged aeroelastic results from mesh independence test.
(V_0=11.4m/s, Ω = 12.1 rpm, θ_p = 0°)

Δ_{min} [m]	R/Δ_{min} [-]	Thrust [KN]	Power [MW]	Inp [m]	Oop [m]	Torsion [deg]
1.5	42	717.30	5.29	-0.59	5.71	0.09
2.0	**31.5**	**713.90**	**5.24**	**-0.59**	**5.70**	**0.07**
4.0	15.8	714.08	5.20	-0.59	5.76	0.08
8.0	7.9	741.76	5.49	-0.62	5.98	0.15

4. Results and discussions

Since the aerodynamic model and control model have been systematically validated in our previous work Yang et al. [36], we focus on the validation of structural model and coupled aero-servo-elastic model in **section 4.1**. Then, the validated aero-servo-elastic model is applied for simulation of a controlled NREL 5MW wind turbine with elastic blades under specified surge motion in **section 4.2**.

4.1 Validations

4.1.1 Test of a static blade

Prior to conducting more complicated aero-servo-elastic simulations, it is beneficial to first validate the structural model in static conditions. The in-plane, out-of-plane and torsional deformations of a single static NREL 5MW wind turbine blade under uniformly distributed loads are compared with results of BeamDyn (stand-alone version v1.01[46]) in **Fig. 9**. The first six natural frequencies are listed in **Table 4** with the results using Modal methods[42], GEBT[41], BeamFOAM[24], BModes[47] and ABQUS[47]. The lowest three modal shapes are compared in **Fig. 10** with FAST results[2].Excellent agreements are obtained, indicating that the structural model is well established.

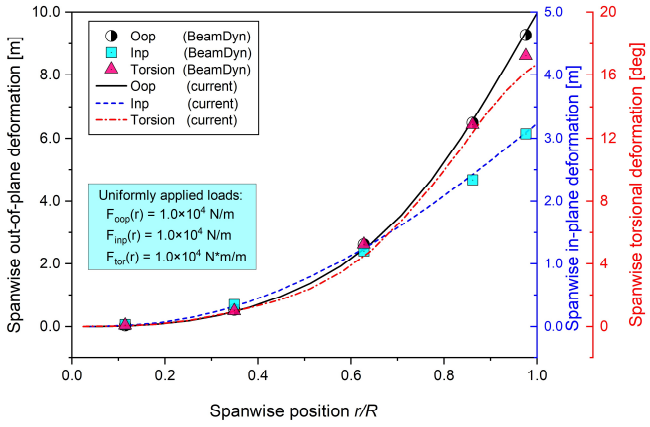

Fig. 9. Spanwise static deformations under uniform applied loads.

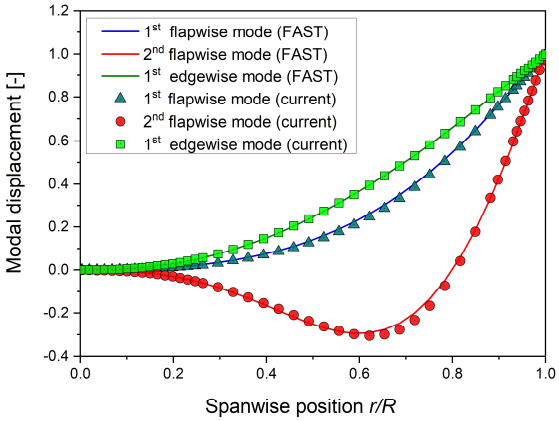

Fig. 10. Modal shapes validation for static NREL 5MW wind turbine blade.

Table 4 Natural frequencies (Hz) of a single blade without applied loads and rotation.

No.	Current	Modal[42]	GEBT[41]	BeamFOAM[24]	BModes[47]	ABAQUS[47]
f_{n1}	0.70	0.68	0.68	0.67	0.69	0.68
f_{n2}	1.11	1.09	1.10	1.06	1.12	1.10
f_{n3}	2.02	1.95	1.98	1.91	2.00	1.98
f_{n4}	4.12	4.00	3.99	-	4.12	3.99
f_{n5}	4.67	4.52	4.66	-	4.64	4.66
f_{n6}	5.58	5.58	5.53	-	5.61	5.53

4.1.2 Stiffening of a rotating uniform cantilever beam

Since the blades are modeled as rotating cantilever beams in this paper, a rotating uniform cantilever beam is herein used to partially validate the structural model in predicting rotation added centrifugal-stiffening effects. The mass density (ρ_s) of the uniform beam is 7840 kg/m^3, cross-section area (A) is $2.0 \times 10^{-4}\ m^2$, elastic modulus (E) is $2.0 \times 10^{11}\ Pa$, cross-section moment of inertial (I) is $2.0 \times 10^{9}\ m^4$, and beam total length (L) is $0.6m$. In simulation, the uniform beam is divided into 50 elements, and only the centrifugal-stiffening effects are considered in order to be consistent with the reference case setups. For better comparations, the dimensionless angular velocity (γ) and natural frequency (μ) are introduced as

$$\gamma = \Omega \sqrt{\frac{\rho_s A L^4}{EI}} \quad \text{and} \quad \mu = \omega \sqrt{\frac{\rho_s A L^4}{EI}}, \tag{21}$$

where Ω is angular velocity (rad/s), ω is circular natural frequency.

The lowest three dimensionless natural frequencies for $\gamma = 0, 1, 5$ and the lowest three modal shapes for $\gamma = 0$ and 12 are compared in **Table 5** and **Fig. 11**, respectively. The current results

agree well with the results of Gebhardt and Roccia[48] using nonlinear finite element beam method and the exact solutions from Wright et al.[49] using convergent power series, indicating the centrifugal stiffening effects are correctly modelled.

Table 5 Comparation of dimensionless natural frequencies of a rotating uniform cantilever beam

γ	Mode	Current	Gebhardt and Roccia[48]	Wright et al.[49]
0	First	3.5159	3.5160	3.5160
	Second	22.0337	22.0345	22.0345
	Third	61.6951	61.6972	61.6972
1	First	3.6815	3.6816	3.6817
	Second	22.1802	22.1810	22.1810
	Third	61.8396	61.8418	61.8418
5	First	6.4490	6.4495	6.4495
	Second	25.4447	25.4460	25.4461
	Third	65.2023	65.2051	65.2050

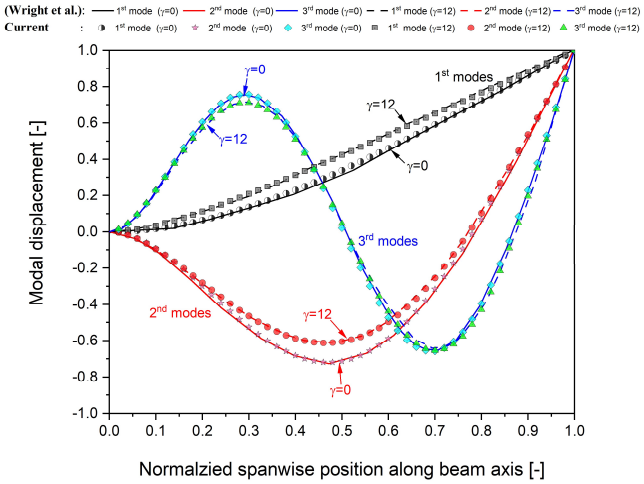

Fig. 11. Modal shapes validation for a rotating uniform cantilever beam at $\gamma = 0, 12$.

4.1.3 Validations for coupled aero-servo-elastic model

In this sub section, the coupled aero-servo-elastic performances of a bottom-fixed NREL 5MW wind turbine under uniform inflow conditions are validated. The significance of aerodynamic center offset effects on torsional deformation is particularly highlighted. The mean results are averaged over the last rotor revolution when the time histories reach steady states. Blade pitch control with constant power mode in region 3 (see **Fig. 6**) is used.

In **Fig. 12** , the rotor thrust, rotor power, blade tip Oop and Inp deformations at wind speeds ranging from 4 m/s to 24 m/s are cross validated with Jonkman et al.[2] using modal methods (FAST ElastDyn), Rodriguez and Jaworski[40] using free vortex wake method with nonlinear

finite element method (FVM-FEM), Ma et al.[30] using actuator line method with nonlinear finite element beam model(ALFBM) and Leng et al. [32] using actuator line method with geometrically exact beam theory(ALM-GEBT). The results of FAST with BeamDyn (open-FAST v2.3.0) are also added for comparation.

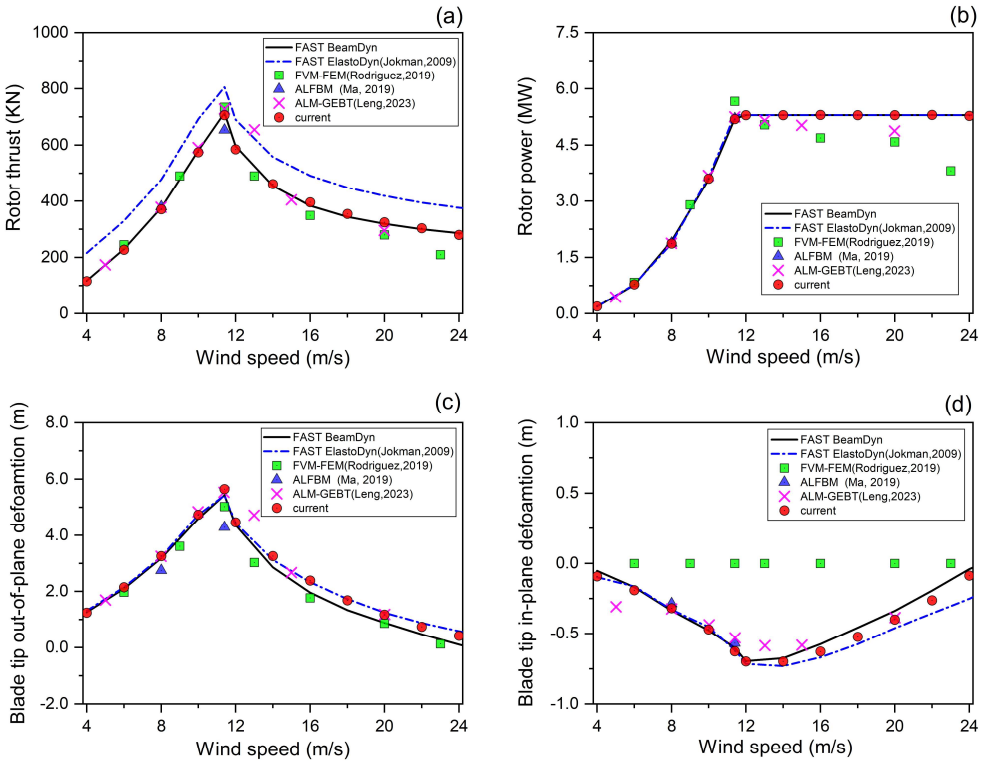

Fig. 12 . Azimuth-averaged rotor performances and blade tip deflections with varying wind speeds: (a) rotor thrust, (b)rotor power, (c) out-of-plane and (d) in-plane deformations.

Excellent agreements are observed for the current results with FAST BeamDyn in terms of rotor thrust and power. The constant power feature at above-rated wind speeds is well captured thanks to the inclusion of control module. The thrust overprediction in Jonkman et al.[2] is due to the definition of "RotThrust" in FAST which is the total force of rotor acting on the tilted shaft, including aerodynamic force, gravity component (approximately 94KN for tilt angle of 5°) and inertial effects. The blade tip Inp and Oop deformations are slightly varied between FAST ElastoDyn and FAST BeamDyn at above-rated wind speeds. This can be explained by the different modelling methodologies on blade torsion, wherein ElastoDyn totally neglects torsion effects, BeamDyn considers the coupling between torsion and bending shear while the current

method models torsion as an independent DOF.

Since the blade torsional deformations and blade pitch angles directly impact the sectional effective AOAs, a detailed discussed is followed with an emphasize on aerodynamic center offset effects. The results from FAST with BeamDyn and Yu et al.[17] using CFD-CSD as well as Jeong et al.[47] using BEM-ABAQUS are compared in **Fig. 13** , wherein the data with "No.AC" indicates no aerodynamic center offset.

As shown, the current results agree well with FAST BeamDyn for conditions with and without AC offset. Significant discrepancies are observed for blade torsion near the rated wind speeds for cases with and without AC offset (**Fig. 13 (a)**). Without AC offset, the large (in terms of magnitude) nose-down torsional deformations can result in significantly reduced AOAs and consequently the rotor performances near rated wind speeds, and the blade pitch angles required to maintain rated power at above conditions are reduced (See **Fig. 13 (b)**). To further examine the AC offset effects, the spanwise torsional deformations at rated wind speeds are plotted in **Fig. 14** with additional results from Imiela et al. [50] and Dose et al.[24] using CFD-CSD, Li et al.[41] using BEM-GEBT, and Leng et al.[32] using ALM-GEBT. The current method reproduces the spanwise torsions well for cases without AC offset (**Fig. 14 (a)**). Although the predicted spanwise torsions are slightly varied for cases with AC offset (**Fig. 14 (b)**) which may due to different structural models and geometry preparations, the magnitudes are small and should not have considerable impact on rotor performances and wake features. The reason why the results of Yu et al. [17]using CFD-CSD show similar magnitudes with other results without considering AC offset is unclear. The azimuth-averaged spanwise blade deflections are also well predicted as shown in **Fig. 15**.

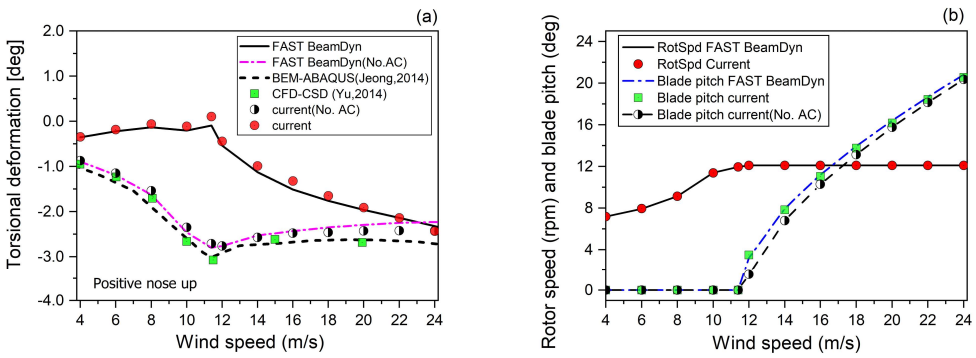

Fig. 13. Azimuth-averaged (a) blade tip torsional deformation, (b) rotor speed and blade pitch angle with varying

wind speeds.

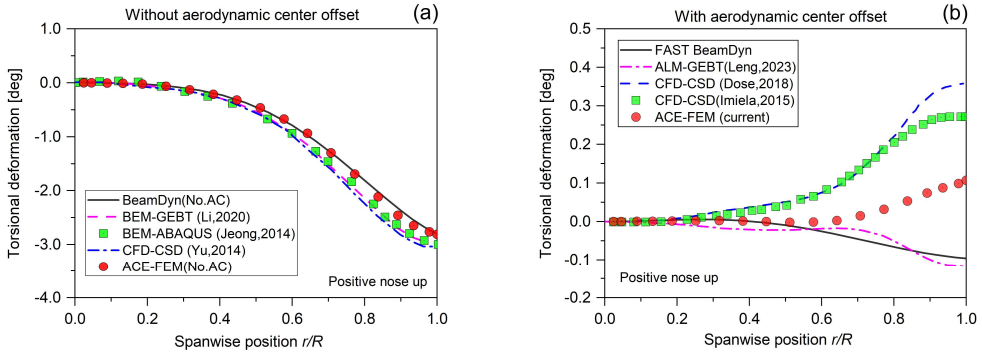

Fig. 14. Azimuth-averaged spanwise blade torsional deformations at rate wind speed. (a) without AC offset;(b) with AC offset.

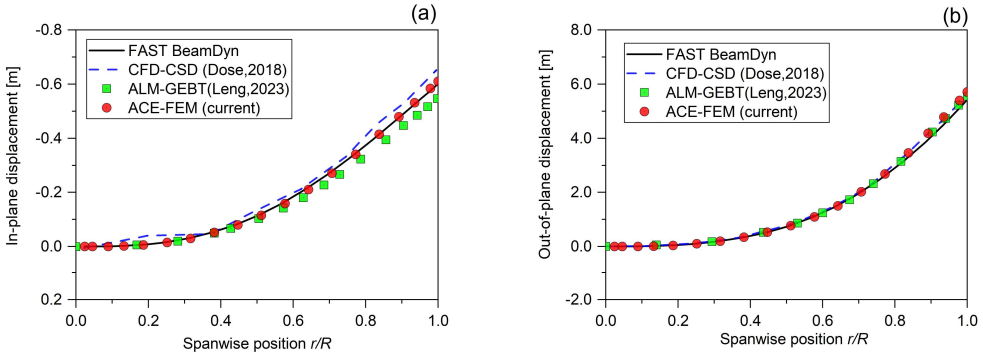

Fig. 15 Azimuth-averaged spanwise blade deflections at rated wind speed: (a) Out-of-plane deformations, (b) In-plane deformations.

A comprehensive comparation of rotor performances and blade tip deformations at rated wind speed is presented in **Table 6**, wherein the current results show the rotor thrust and Oop deformation are greatly influenced by AC offset effects which are decreased by 10.5% and 15.0%. Meanwhile, the current rotor thrust and power are only slightly decreased by 1.0% and 0.2% comparing with BeamDyn, which indicates the AC offset effects are far more significant than geometry nonlinearities and the usage of Euler-Bernoulli beam with various nonlinear effects is acceptable at least for the current 5MW-class wind turbine at rated condition.

Table 6 Comparation of Azimuth-averaged rotor performances and blade tip deformations of the NREL-5MW RWT at rated wind speed.

Study	Model	Year	Inp (m)	Oop (m)	Torsion (deg)	Thrust (KN)	Power (MW)
Jonkman et al.[2]	BEM-Modal	2009	-0.61	5.47	-	814.45	5.28
Yu and Kwon[17]	CFD-CSD	2014	-0.63	**4.72**	-3.04	**656.43**	5.22
Li et al.[19]	CFD-MBD	2015	-0.58	6.38	-	759	5.41
Imiela and Wienke[50]	CFD-CSD	2015	-0.65	5.98	0.28	808	5.62
Ponta et al.[51]	BEM-GTBM	2016	-0.56	**3.85**	-	**660.19**	5.19

Dose et al.[24]	CFD-CSD	2018	-0.64	5.98	0.29	768.60	5.46
Sabel and Gopal[52]	BEM-GEBT	2019	-0.57	4.41	-0.29	690.72	4.97
Sabel and Gopal[53]	BEM-GEBT	2019	-0.62	4.55	-	676.12	5.17
Ma et al.[30]	ALM-Beam	2019	-0.57	**4.28**	-	**653**	5.20
Liu et al.[20]	CFD-MBD	2019	-0.60	5.60	-	733.00	4.90
Li et al.[41]	BEM-GEBT	2020	-0.57	**4.49**	-2.97	**678.44**	5.30
Leng et al.[32]	ALM-GEBT	2023	-0.55	5.53	-0.12	728.50	5.26
Zheng et al.[33]	ALM-Beam	2023	-0.28	4.95	-	681.64	4.67
BeamDyn(No.AC)	BEM-GEBT	2023	-0.59	4.69	-2.80	651.51	5.08
BeamDyn	BEM-GEBT	2023	-0.60	5.43	-0.10	713.37	5.20
Current (No.AC)	ACE-Beam-PI	2023	-0.53	4.80	-2.71	632.21	4.92
Current	ACE-Beam-PI	2023	-0.62	5.65	0.10	706.10	5.19

For completeness, the results of different blade types and control configurations are summarized in **Table 7**. Blade elasticity is found to slightly reduce the rotor performances for no-controller cases (case 1 and 3) and the controller responses (rotor speed and blade pitch) for with-controller cases (case 2 and 4) which leads to an increase of rotor thrust is by 3.4%. For rigid and elastic blades, the controller tends to reduce rotor performances through positive blade pitch angle or reduced rotor speed.

Table 7 Comparation of Azimuth-averaged rotor performances and blade tip deformations of the NREL 5MW RWT at rated wind speed.

Case	Study	Wind speed (m/s)	RotSpd (rpm)	Pitch (deg)	Thrust (KN)	Power (KW)	Inp (m)	Oop (m)	Torsion (deg)
1	Rigid blades	11.4	12.1	0	723.69	5.43	/	/	/
2	Rigid blades + control	11.4	12.1	**0.84**	683.20	5.30	/	/	/
3	Elastic blades	11.4	12.1	0	714.53	5.25	-0.59	5.70	0.08
4	Elastic blades + control	11.4	**11.8**	0	706.10	5.19	-0.62	5.65	0.10

The azimuthal variations of blade tip deflections over the last revolution are shown as polar-theta plots in **Fig. 16**, where zero theta indicates blade vertical up. The maximum Inp deflections (in terms of magnitude) is observed at theta of 90° where the gravity-induced torque reaches maxima and acts in the same direction of aerodynamic torque, while the minimum Inp is observed at theta of 270° where the maximum gravity-induced torque and aerodynamic torque act in opposite directions.

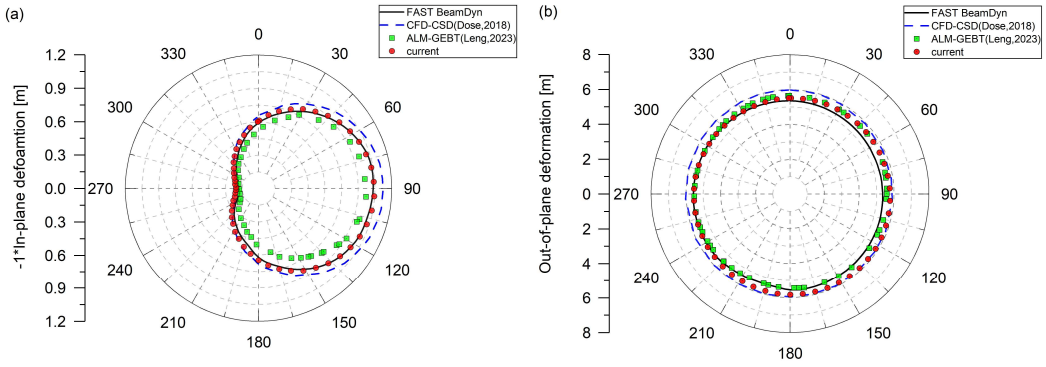

Fig. 16. Azimuthal variation of blade tip (a) in-plane (multiplied by -1) and (b) out-of-plane deformations at rated wind speed.

Based on the above validations, it is evident that the proposed aero-servo-elastic method is well established and can be further applied for coupled aero-servo-elastic wake behavior analysis of controlled floating offshore wind turbine(s).

4.2 Surge motion cases

The platform surge displacement X_S is specified as sinusoidal functions as: $X_S(t) = A_S \sin(2\pi f_s t)$ and the platform surge velocity is therefore : $V_S(t) = 2\pi f_s A_s \cos(2\pi f_s t)$, wherein the A_S and f_s are surge amplitude and surge frequency. The normal inflow velocity relative to the rotor plane is $V_c = V_0 - V_S$. To better analyze the coupled aero-servo-elastic responses and wake features of a FOWT under specified surge motions, eight typical time instants (T_0~T_7) are introduced (see **Fig. 17**), wherein the platform moves toward downstream from the equivalent position at T_0 to the downstream-most position at T_2, and then moves back to the equivalent position at T_4, and further reaches the upstream-most position at T_6. The minimum and maximum normal inflow velocity V_C happens at T_0 and T_4, respectively.

Following the work of Lienard et al.[54] , the surge frequency f_S is chosen to allow the rotor to rotate two revolutions with rated rotor speed of 12.1 rpm during one surge period, so that the $f_s = 12.1/120 = 0.10083$ Hz which falls in typical wave frequency range 0.05~2.0 Hz, while a smaller surge amplitude of $A_s = 4m$ is used.

In this sub section, four cases (A_1,A_2,A_3 and A_4) are performed to demonstrate the capabilities of the proposed aero-servo-elastic method for fluid-structure interaction simulations of a

controlled FOWT under specified surge motion. In case A_3 and A_4, the rotor speed control is combined two respective blade pitch control strategies, constant power mode and constant torque mode, wherein the first one seeks to maintain the rated generator power in region 3 while the second one maintains rated generator torque in region 3. The detailed case setups are listed in **Table 8** with additional aims to quantify the effects of blade elasticity and control strategies on the aero-servo-elastic responses as well as wake characteristics.

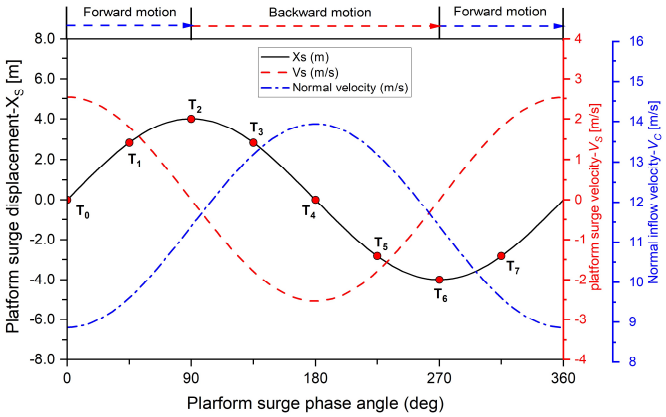

Fig. 17. Platform surge motion description[36].

Table 8 Platform surge motion parameters and rotor operating conditions. The values of V_0 , Ω , θ_p describe the inflow wind speed, rotor speed and blade pitch angle. The symbols A_S and f_s represent the surge motion amplitude and frequency.

Case	Model	$V_0\ [m/s]$	$\Omega\ [rpm]$	$\theta_p[°]$	$A_S[m]$	f_s [Hz]
A_1	Surge + rigid blades	11.4	12.1	0	4	0.10083
A_2	Surge + elastic blades	11.4	12.1	0	4	0.10083
A_3	Surge +elastic blades + constant power	11.4	dynamic	dynamic	4	0.10083
A_4	Surge +elastic blades + constant torque	11.4	dynamic	dynamic	4	0.10083

4.2.1 Unsteady loads and responses

In **Fig. 18**, the unsteady rotor thrust, rotor power, rotor speed and collective blade pitch angle are plotted as functions of platform surge displacement. Without control strategy (case A_1 and A_2), the rotor loads show as elliptical hysteresis loops with the minima and maxima at T_0 and T_4. For case A_2, the thrust varies from 493.64 KN to 904.20 KN while the rotor power varies from 2.50 MW to 8.52 MW. The differences between case A_1 and A_2 are small, indicating limited effects of blade elasticity on rotor loads. In contrast, the control strategy significantly alters the rotor loads

not only in terms of extreme values but also the evolution patterns. For case A_3, the minimum thrust (31.70 KN) is observed at T_6 as the blade pitch angle reaches maxima of 8.97° while the maximum thrust between T_2 and T_4 of 969.48 KN which coincides with the trigger of blade pitch controller. The constant torque control mode (case A_4) predicts smaller blade pitch angle and thus higher rotor loads from T_6 to T_0 (excluding the range with zero blade pitch) than constant power mode (case A_3), leading to increased mean rotor thrust from 524.56 KN for case A_3 to 539.42 KN for case A_4. The results show it is important to include control strategies for aerodynamic analysis of floating offshore wind turbines.

It should be noted that the blade pitch controller does not trigger and turn off immediately as the rotor speed exceeds or falls below the rated one since the control region identification is based on filtered generator speed ($\widetilde{\Omega}_{gen} = N_{Gear}\widetilde{\Omega}$) instead of the real-time one which is proportional with real-time rotor speed ($\Omega_{gen} = N_{Gear}\Omega$).For case A_3 from T_2 to T_4, the rotor speed exceeds rated value at $X_S = 2.45\ m$ while the pitch controller starts to function at $X_S = 1.06\ m$, corresponding to a surge phase-lag of 22° which is introduced by the low-pass filter (see **Eq. (18)**). The pitch controller is always activated as the pitch angle is positive regardless of the value of filtered generator speed, and the minimum blade pitch angle is set to zero.

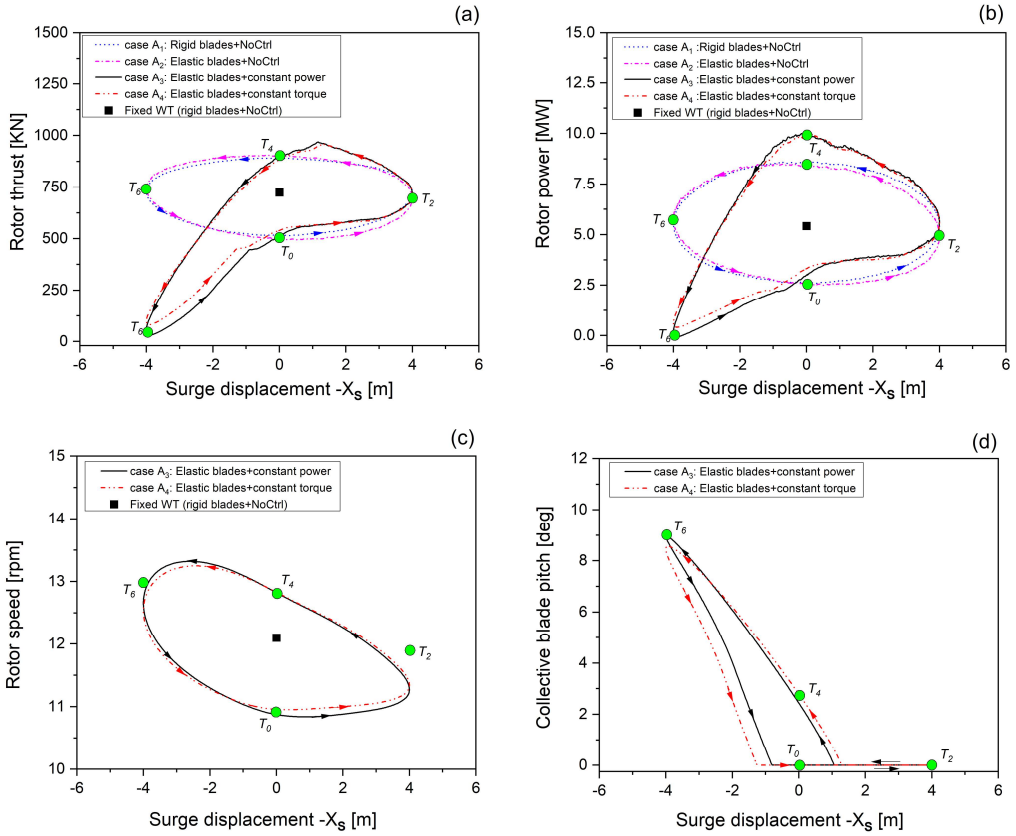

Fig. 18. Rotor performances and controller responses as functions of platform surge displacement: (a) rotor thrust, (b) rotor power, (c) rotor speed and (d) collective blade pitch angle.

Platform surge and pitch motions are greatly influenced by rotor thrust in real applications so that a deeper investigation on thrust is presented. The unsteady rotor thrust can be approximated by first-order Taylor expansion as

$$T_x = T_0 - \frac{\partial T_x}{\partial V_s}\dot{X}_S \tag{22}$$

where T_0 is the reference thrust which is chosen as the mean aerodynamic thrust in this paper. $\frac{\partial T_x}{\partial V_s}$ is thrust sensitivity against platform surge velocity which is a direct estimation of the platform surge aerodynamic damping. For small platform-pitch angles, the platform-pitch damping is $L_{HH}^2 \frac{\partial T_x}{\partial V_s}$ as shown by Jonkman[55] wherein L_{HH} is the vertical distance between hub height and platform-pitch rotational center. The platform-surge aerodynamic damping $\frac{\partial T_x}{\partial V_s}$ can be estimated as the slope of the steady response of $\Delta T = -(T_x - T_0)$ versus V_S as in **Fig. 19**.

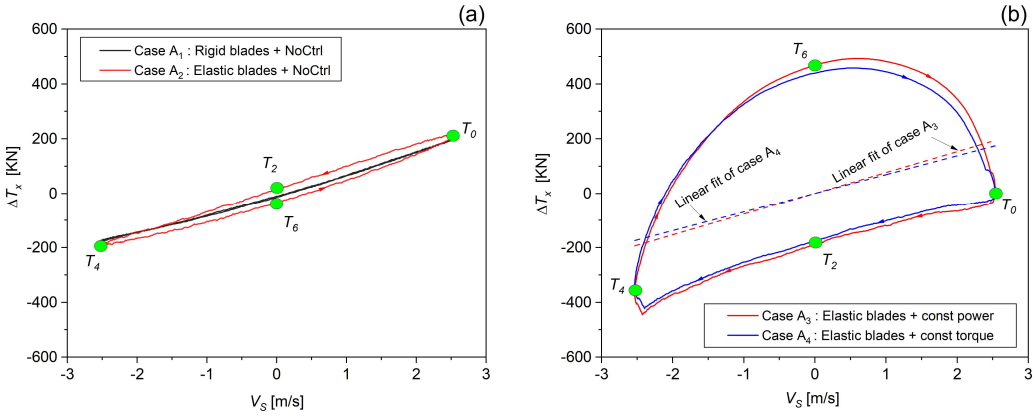

Fig. 19. The oscillating aerodynamic thrust versus platform surge velocity.

An alternative to quantify the aerodynamic damping is using the energy dissipation coefficient following the work of Apsley and Stansby[56] as

$$C_{diss} = -\frac{W_0}{\frac{1}{2}\rho A V_0^2 V_0 T_s} \tag{23}$$

where $A = 0.25\pi D^2$ is rotor sweep area. V_0 is inflow velocity. W_0 is the energy transferred from airflow to the oscillating rotor during one surge period which can be calculated as

$$W_0 = -\int_t^{t+T_s} T_x V_S dt = -\int_{-A_S}^{A_S} (T_x^U - T_x^D) dx_S \tag{24}$$

where T_x^U and T_x^D is the thrust when the rotor moves upstream and downstream, respectively. And $d_{x_S} = V_S dt$.The minus sign is introduced to keep the conventional concept that a system is positively damped if it dissipates energy to airflow. **Eq. (24)** further indicates the value of W_0 is exactly the area of thrust hysteresis loops in **Fig. 19** where counterclockwise loops indicate positive aerodynamic damping. Combining **Eq**. **(22), (23)** and **(24)**, a simple approximate relationship between C_{diss} and normalized thrust sensitivity ($\frac{\partial C_T}{\partial \bar{V}_S}$) can be derived as

$$C_{diss} = \frac{1}{2}\frac{V_{S0}}{V_0}\frac{\partial C_T}{\partial \bar{V}_S} \tag{25}$$

where $V_{S0} = 2\pi f_S \cdot A_S$ is the maximum surge velocity. $\bar{V}_S = V_S / V_{S0}$ is the normalized surge velocity and $C_T = T_x / \frac{1}{2}\rho A V_0^2$ is thrust coefficient.

The $\frac{\partial T_x}{\partial V_s}$ and C_{diss} are listed in **Table 9** together with statistical rotor thrusts and rotor powers. The blade elasticity leads to the increase of $\frac{\partial T_x}{\partial V_s}$ by 7.84% (comparing case A_2 to A_1) while the two

control strategies are shown to decrease the $\frac{\partial T_x}{\partial V_s}$ by 3.90% and 13.56% (comparing case A_3 and A_4 to case A_2). The relative differences calculated using C_{diss} are not identical with those calculated using $\frac{\partial T_x}{\partial V_s}$ because **Eq. (22)** is just a first-order approximation to rotor thrust so that **Eq. (25)** is only valid for ideal conditions where the oscillating thrust is fully in-phase with surge velocity. Either $\frac{\partial T_x}{\partial V_s}$ or C_{diss} in this paper is just an overall estimation of the rotor aerodynamic damping effects during one surge period while the real aerodynamic damping can vary with time.

Table 9 Rotor thrust, rotor power, thrust sensitivity and rotor energy dissipation coefficient for all cases. Results in parenthesis are relative differences between A_2 to A_1, and between A_3 and A_4 to A_2.

Case	Rotor thrust [KN]			Rotor power [MW]			$\frac{\partial T_x}{\partial V_s}$ [KN/m·s^{-1}]	C_{diss} [-]
	Min	Max	Mean	Min	Max	Mean		
A_1	514.26	891.96	713.39	2.60	8.61	5.53	73.93	0.02118
A_2	493.64	904.20	709.25	2.50	8.52	5.42	79.73 (+7.84%)	0.02257 (+6.56%)
A_3	31.70	969.48	524.56	-0.06	10.00	4.50	76.62 (-3.90%)	0.02171 (-3.81%)
A_4	81.57	961.31	539.42	0.41	9.95	4.59	68.92 (-13.56%)	0.01952 (-13.51)

The rotor power variation range of case A_3 (-0.06 MW to 10.00 MW) is much wider than that of the no-controller case A_2 (2.50MW to 8.52MW), which may be counterintuitive as most control strategies are initially designed to save turbine from overloads at above-rated conditions. To clarify this, the concepts of rotor power and generator power should be distinguished. Rotor power is the energy extracted by rotor from airflow in unit time while generator power is the energy absorbed by generator from rotor in unit time, which are calculated as $P_{rotor} = T_a\Omega$ and $P_{gen} = \eta T_{Gen}\Omega_{Gen}$, respectively. The aerodynamic torque T_a is calculated in ACE module while the generator torque T_{Gen} is obtained through the tabulated relationship (see **Fig. 6**). It is the generator power not the rotor power that is directly regulated by control strategies. **Fig. 20** shows the time histories of rotor power and generator power wherein the maximum generator power of case A_3 and A_4 are well regulated to near the rated 5.0 MW.

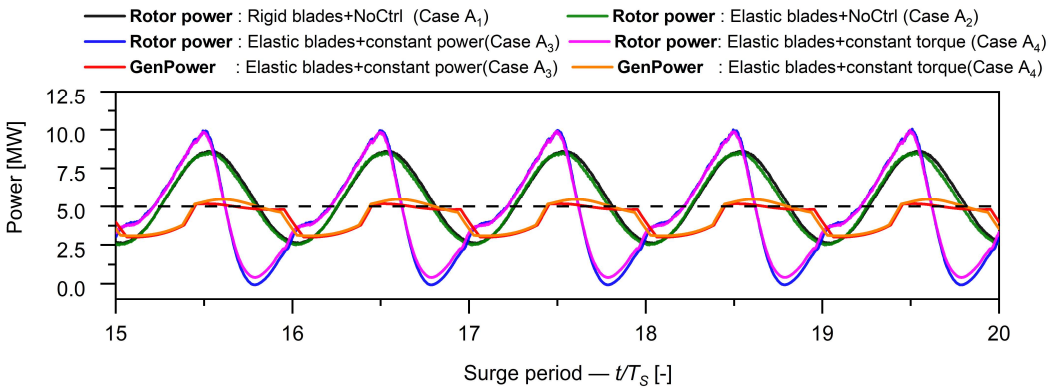

Fig. 20. Time histories of rotor power and generator power.

The blade tip out-of-plane (Oop) and torsional deformations show as similar steady hysteresis loops (**Fig. 21**). The minimum Oop and torsional deformations of case A_3 and A_4 are observed at T_6 with minimum rotor thrusts and the aerodynamic center offset induced sectional aerodynamic moments. The mean Oops and blade torsions are consistent with the trends of mean rotor thrust. Moreover, the maximum Oops are 6.96m, 7.56m and 7.52m for cases A_2, A_3 and A_4, indicating the surge motion and control strategies can possibly lead to stronger blade-tower interactions and increase the risks of tower strike. The high-frequency oscillations in **Fig. 21(b)** relate to the natural frequencies of blade torsion. The blade tip in-plane deformations with control strategies are not strictly periodic steady so that they are plotted as time histories in **Fig. 22**. It shows the control strategies only slightly influence the maximum and minimum in-plane deformations but allow for the high-order frequencies to be excited.

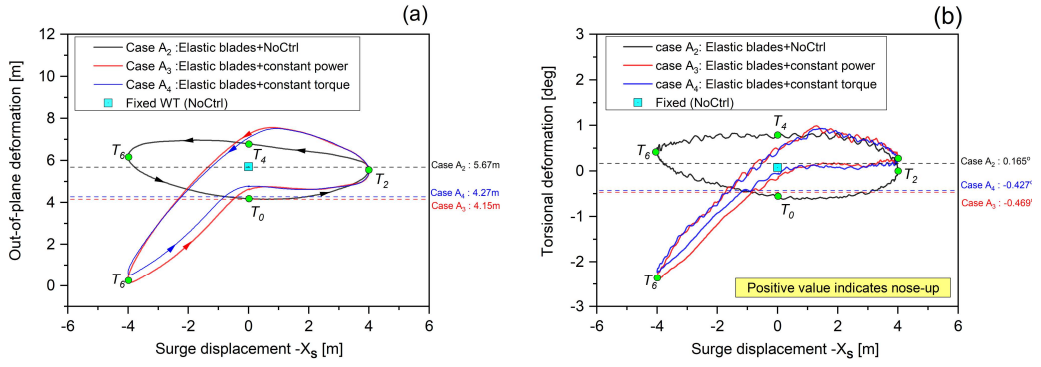

Fig. 21. Blade tip out-of-plane and torsional deformations as functions of platform surge displacement: (a) Out-of-plane deformation and (b) blade torsion.

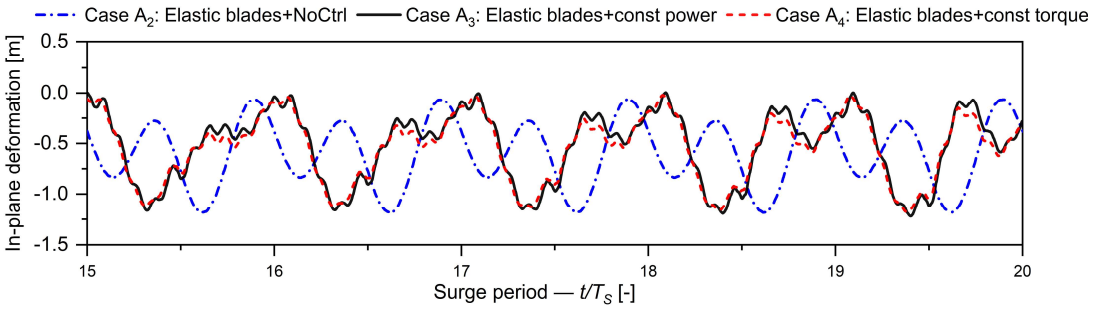

Fig. 22. Time histories of blade tip in-plane deformations.

4.2.2 Wake characteristics

In **Fig. 23,** the wake vortex structures are visualized via the Q-criterion[57, 58], wherein Q is the second invariant of velocity gradient tensor and is defined as $Q = -\frac{1}{2}(u_{i,i}^2 - u_{i,j}u_{j,i})$. The helical tip vortices in near wake regions are transitioned and merged into a set of vortex rings. This is due to the fact that the tip vortices are released from blade tips with different initial streamwise velocities during one surge period, so that the vortex-vortex interactions lead to the formation of vortex rings. The vortex ring structures are greatly impacted by the inclusion of control strategies while the differences between two control types are negligible. **Fig. 24** shows blade elasticity accelerates the formation of the fist vortex ring structure (see the dashed boxes in **Fig. 24 (a)** and **(b)**) due to blade elastic vibrations, and control strategies significantly reduce the core size of the vortex rings. The rapid diffusion of wake vortices in far wake is due to the large streamwise grid resolution as the wake refinement region only extends to $5D$ downstream.

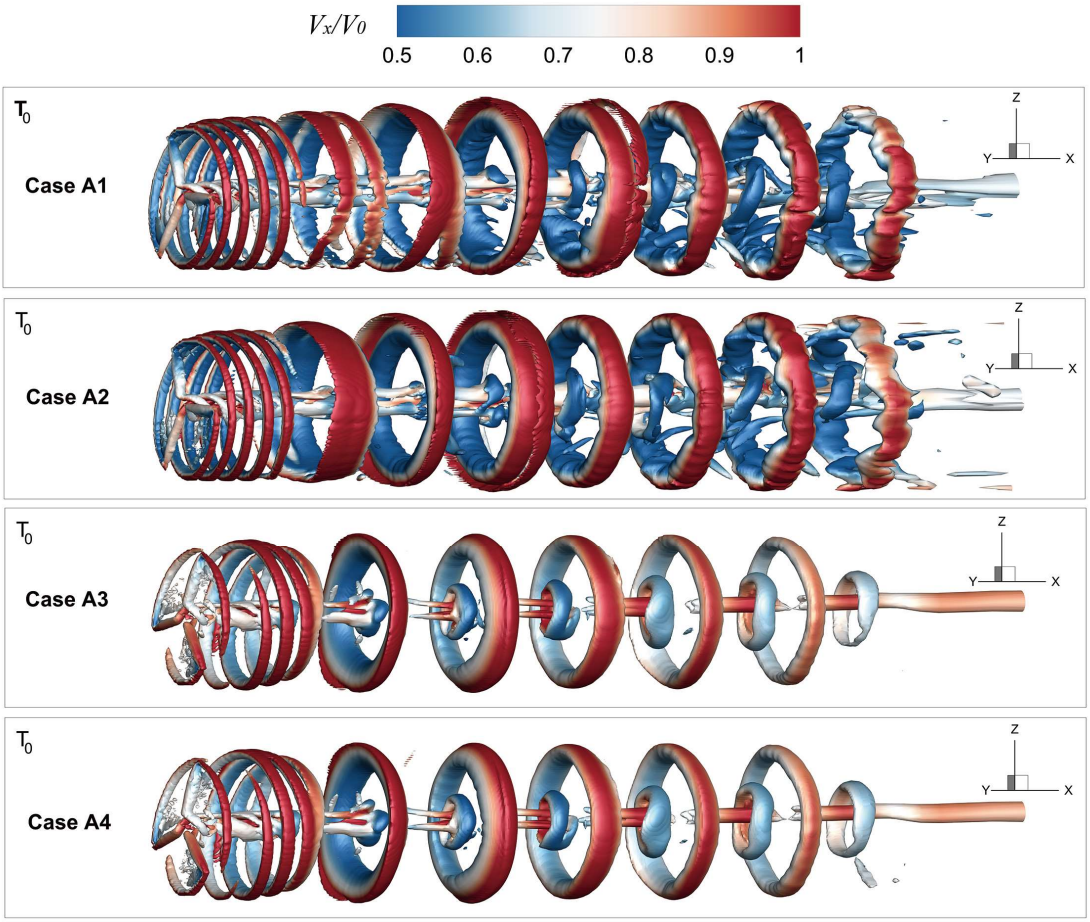

Fig. 23. Wake vortex structures at T_0 (visualized by $Q = 0.01$ and colored by normalized streamwise velocity).

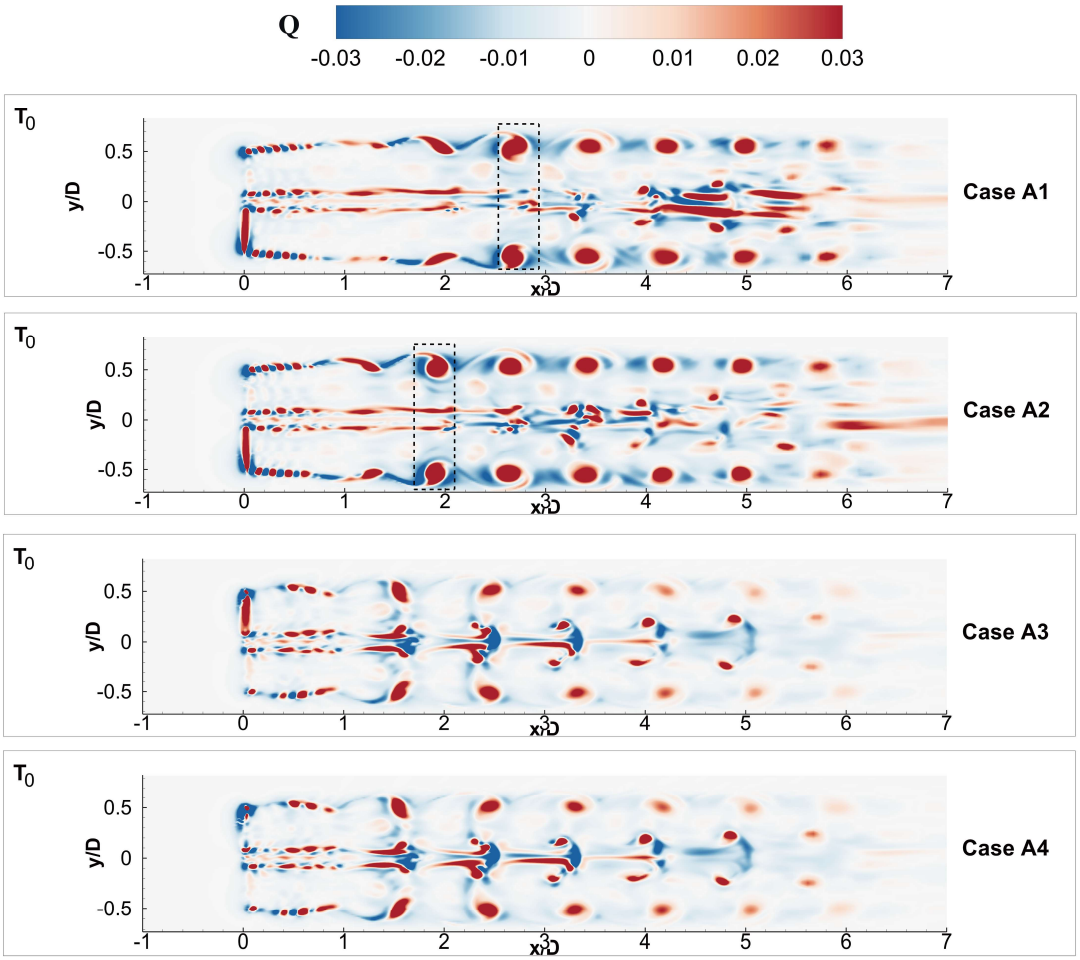

Fig. 24. Instantaneous Q field in xy plane at hub height at T_0 for cases A_1, A_2, A_3 and A_4.

To further quantify the wake characteristics, the streamwise velocities (V_x) are probed along lateral directions (y direction) at hub height (Z=90m) for five downstream positions $x/D = 1, 2, 3, 4, 5$ and time averaged over the last two surge periods (19-20) in order to calculate the dimensionless mean velocity deficits as $\frac{\Delta\bar{V}_x}{V_0} = 1 - \frac{\bar{V}_x}{V_0}$ which are plotted in **Fig. 25**. The $\frac{\Delta\bar{V}_x}{V_0}$ at $x/D = 5$ is further transversely averaged between $-0.7 < y/D < 0.7$ to assess the overall far wake deficit and the results for case A_1, A_2, A_3 and A_4 are 0.370, 0.360, 0.223 and 0.232, respectively. The overall far wake deficit is decreased by 2.7% from 0.370 for case A_1 to 0.360 for case A_2, showing the blade elasticities slightly accelerate the far wake recovery. While the two control strategies were found to significantly reduce the overall far wake deficits by 38.1% and 35.6% comparing case A_3 and A_4 to case A_2. This is because the minimum blade pitch angle is set as 0° for the current pitch controller. When the filtered rotor speed is above rated value, the pitch

controller introduces positive pitch angle and thus less power extraction. However, when the filtered rotor speed is below the rated value, the blade pitch angle is maintained as 0° instead of being negative ones to increase power extraction. As a result, the rotor extracts much less energy during one surge period compared with the no controller cases, thus the mean wake deficits are greatly reduced.

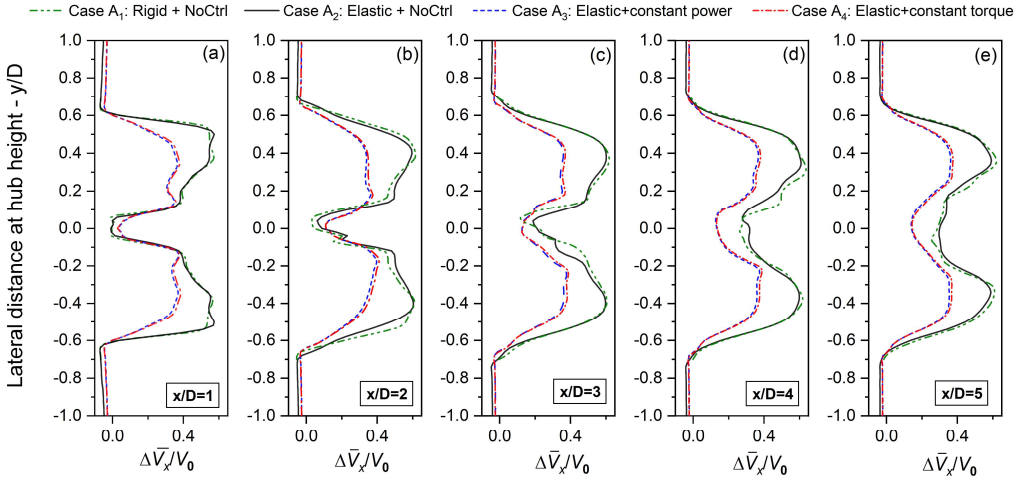

Fig. 25. Time-averaged dimensionless streamwise velocity deficit ($\Delta\bar{V}_x/V_0$) at hub height along lateral direction at downstream positions of $x/D = 1, 2, 3, 4, 5$.

5. Summary and conclusion

In this paper, a new numerical method is proposed for coupled aero-servo-elastic analysis of floating offshore wind turbines including wakes. The method is based on solving incompressible Navier-Stokes Equations on stretching Cartesian grids using finite difference method. The effects of rotating blades on flow are modeled as body force terms using Actuator Curve Embedding method and a nonlinear finite element rotating beam theory is adopted for blade elasticity modeling. Both generator torque control and collective blade pitch control strategy are considered. The novelty of this method is that it is capable for efficient aero-servo-elastic simulations of FOWT(s) including wakes on coarse Cartesian grids without requiring empirical tip loss corrections. Systematic validations were performed and the aero-servo-elastic loads and wakes of a NREL 5MW wind turbine under platform surge motion were analyzed using the current new

method. The major conclusions are as follows:

- The proposed aero-servo-elastic method is well-established and can accurately predict rotor performances, blade natural frequencies, modal shapes, elastic deformations and controller responses with affordable computational cost.
- Aerodynamic center offset effects are essential for accurate aero-servo-elastic predictions. If neglected, the magnitude of blade tip torsion can be overpredicted by 26.1 times (comparing $-2.71°$ to $0.1°$) for the NREL 5MW wind turbine at rated conditions, leading to the rotor thrust and blade tip out-of-plane deformation being underpredicted by 10.5% and 15.0%, respectively.
- The two control strategies (constant power and constant torque mode) were found to significantly reduce the overall far wake deficit by 38.1% and 35.6%, while blade elasticity only slightly reduces the same quantity by 2.7%. These findings indicate control strategy can be much more influential than blade elasticity on far wake deficits for a floating turbine in particular conditions.
- Compared with the constant power mode, the pitch control with constant torque mode slightly increased the overall far wake deficit by 4.0% which may have some negative effects on downstream turbines.

In future works, more modern IEA 15MW wind turbine, which have more realistic offsets and more significant blade torsional deformations, should be used and the method can be coupled with a floating body dynamic code to establish an aero-hydro-servo-elastic-mooring framework with inflow shear and turbulence in more realistic sea states. With the increasing tower height and blade span, the inclusion of tower flexibility and modeling flexible blades with more advanced geometrically exact beam theory are natural next-steps. Due to the cyclic nature of blade pitch angles and blade elastic vibrations, it would be beneficial to include a dynamic stall model to account for the hysteresis effects of sectional aerodynamic coefficients, especially for a FOWT operating in harsh sea states or wind gust conditions where the current quasi-steady aerodynamic model may fail to predict the high dynamic lift due to the delay of stall.

Appendix A. Special region treatment in ACE

Theoretically, the blade forces are projected in planes normal to the actuator curve. However, the actuator curve is usually represented by a set of discrete segment lines instead of a smooth curve. Thus, the fluid region influenced by an actuator curve can have two special regions on the concave and convex side, which are donated as concave region and convex region with the rest region donated as normal region as shown in **Fig. A.1**. In the concave region, a fluid point can find multiple planes normal to the blade segment lines. While for the fluid points in the convex region, no plane normal to any blade segment line can be find. Therefore, special treatments are required in the two special regions to obtain the required tangential and normal coordinates (r_s and r_n) for ACE implementation. The tangential coordinate is normalized as $p_{s,m} = r_{s,m}/\Delta b_m$ for better following discussions.

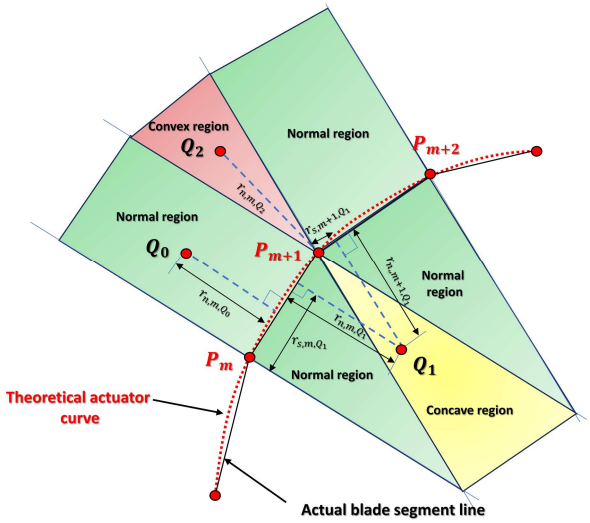

Fig. A.1 Concave and convex cases for ACE.

In HEU-FOWT code, the region type identification and the treatments for each fluid point Q based on the following criterions:

- If only **ONE** element satisfies $p_s \in (0,1]$ (see Q_0 in **Fig. A.1**), then Q is in the normal region, and the r_s and r_n are calculated using this element;
- If **Multiple** elements satisfy $p_s \in (0,1]$ (see Q_1 in **Fig. A.1**), then Q is in the concave region, but only the element with minimum r_n is used for calculating the final r_s and r_n;

- If $p_s \notin (0,1]$ for all elements but have the properties of $p_{s,m} > 1$ and $p_{s,m+1} \leq 0$ (see Q_2 in **Fig. A.1**), then Q is in convex region, and it is associated with the m^{th} element. Special treatments are performed as $p_s = 1.0$ and $r_n = \overline{Q_2 P_{m+1}}$.

A uniformly-loaded (1000N/m) quarter arc curve with four actuator points is used to demonstrate the capabilities of the ACE method in HEU-FOWT code on treating the special regions for an actuator curve with very large deformation. The different regions are well identified (primary values located at the lowest-indexed cell corners) as shown in **Fig. A.2**, and the projected body force field (with $\varepsilon = \Delta = 4$m) in different regions are shown in **Fig. A.3**.

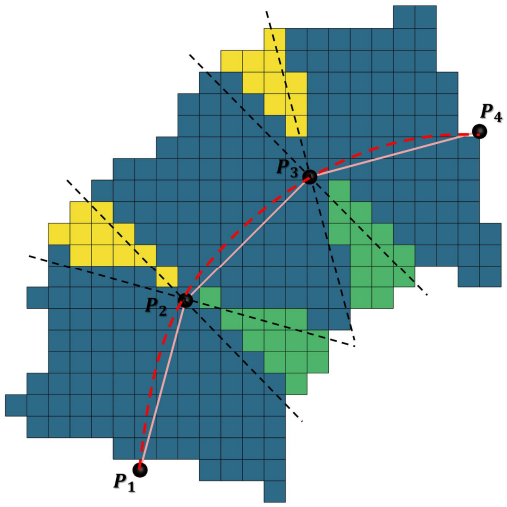

Fig. A.2 Region identification for a quarter arc.
(Yellow: convex region; Green: convex region; Blue: normal region)

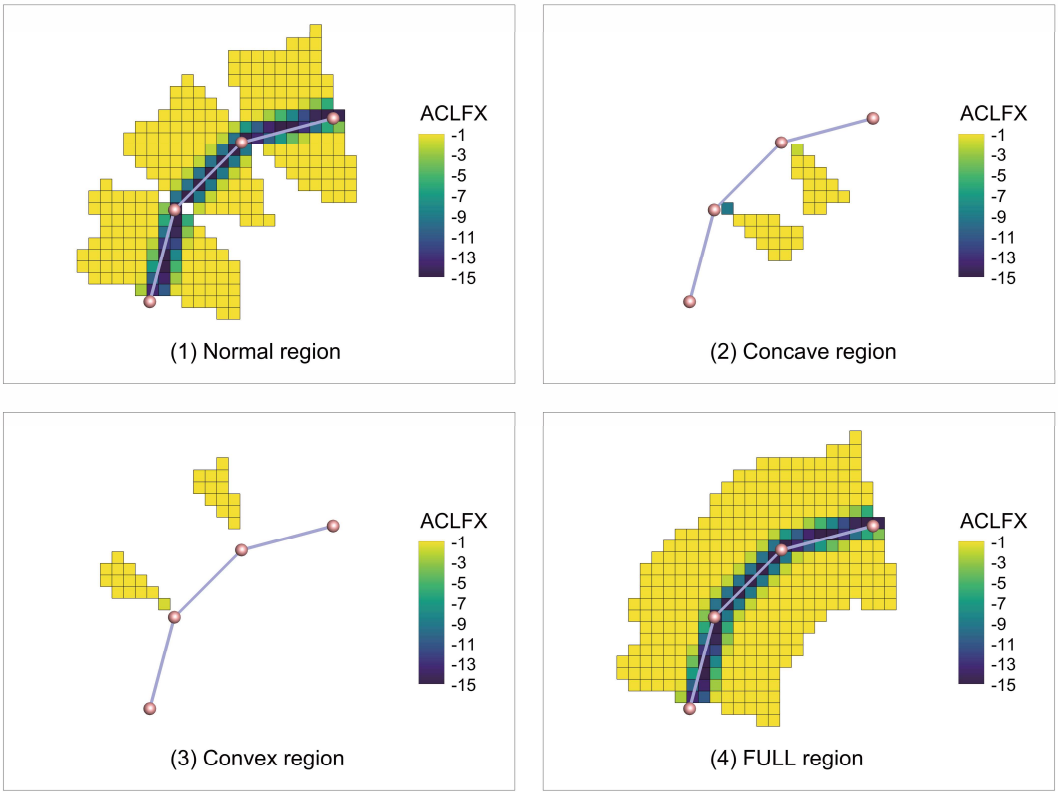

Fig. A.3 Body force field in different regions.

Appendix B. Derivation of the elemental equations of motion

The equation of motion for each blade beam element is derived using Lagrange's equations,

$$-\frac{d}{dt}\left(\frac{\partial \mathcal{T}}{\partial \dot{q}_i}\right)+\frac{\partial \mathcal{T}}{\partial q_i}+\frac{\partial \mathcal{U}}{\partial q_i}=\mathcal{P}_i \tag{B.1}$$

where $\mathcal{T}$ is total kinetic energy, $\mathcal{U}$ is total strain energy, q_i is the i^{th} degree-of-freedom and $\mathcal{P}_i$ is the i^{th} generalize load of the finite beam element. $\dot{q}_i$ is the time derivative of q_i.

The total kinetic energy ($\mathcal{T}$) of a Euler-Bernoulli beam element is simply

$$\mathcal{T}=\frac{1}{2}\int_0^L \rho_s A\left(\dot{u}_x^2+\dot{u}_y^2+\dot{u}_z^2\right)^2 dx+\frac{1}{2}\int_0^L \rho_s J\dot{\theta}_x^2 dx \tag{B.2}$$

where ρ_s is mass density, A is cross-sectional area and J is rotational inertial around local x axis.

The total strain energy ($\mathcal{U}$) due to axial displacement, transverse bending, torsion and axial tension can be modelled using classic rod, beam, shaft and pretensioned cable models as

$$\mathcal{U} = \frac{1}{2}\int_0^L EA\left(\frac{\partial u_x}{\partial x}\right)^2 dx + \frac{1}{2}\int_0^L GJ\left(\frac{\partial \theta_x}{\partial x}\right)^2 dx + \frac{1}{2}\int_0^L \left[EI_z\left(\frac{\partial^2 u_y}{\partial x^2}\right)^2 + EI_y\left(\frac{\partial^2 u_z}{\partial x^2}\right)^2\right] dx + \frac{1}{2}\int_0^L T_x^*\left[\left(\frac{\partial u_y}{\partial x}\right)^2 + \left(\frac{\partial u_z}{\partial x}\right)^2\right] dx \quad \text{(B. 3)}$$

where E is elastic modulus, G is shear modulus, I_y and I_z is the cross-section moment of inertial relative to local y and z axis, respectively. T_x^* is axial tension mainly resulting from the accumulated centrifugal force and gravitational force as

$$T_x^*(x) = \int_x^R \rho_s A[\boldsymbol{\Omega\Omega}(\boldsymbol{r} + \boldsymbol{x^e}) + \boldsymbol{T}\mathbf{g}]dx \cdot [1,0,0]^T \quad \text{(B. 4)}$$

where $\boldsymbol{T}$ is the coordinate transformation matrix from global inertial coordinate system to local blade coordinate system. $\mathbf{g} = [0, 0, -9.81]^T$ is gravitational acceleration. $\boldsymbol{r}$ and $\boldsymbol{x^e}$ are the initial undeformed elemental nodal position and elemental nodal elastic deformation, respectively. The dot product with vector $[1,0,0]^T$ is intended to extract the x component. $\boldsymbol{\Omega}$ is the skew symmetric matrix of the rotor angular speed vector $\boldsymbol{\omega} = [\omega_x, \omega_y, \omega_z]^{\boldsymbol{T}}$ (represented by S_{b_i}) as

$$\boldsymbol{\Omega} = \begin{bmatrix} 0 & -\omega_z & \omega_y \\ \omega_z & 0 & -\omega_x \\ -\omega_y & \omega_x & 0 \end{bmatrix} \quad \text{(B. 5)}$$

Inserting **Eq. (16), (B.2)** and **(B.3)** into **Eq. (B.1)**, the elemental mass matrix ($\boldsymbol{M^e}$), structural stiffness matrix ($\boldsymbol{K^e}$) and stress stiffening matrix ($\boldsymbol{stress^e}$) can be obtained as

$$\boldsymbol{M^e} = \int_0^L \rho_s A \boldsymbol{N_0^T N_0} dx + \int_0^L J \boldsymbol{N_4^T N_4} dx \quad \text{(B. 6)}$$

$$\boldsymbol{K^e} = \int_0^L \boldsymbol{B_0^T S B_0} dx \quad \text{(B. 7)}$$

$$\boldsymbol{stress^e} = T_x^* \int_0^L \boldsymbol{B_1^T B_1} dx \quad \text{(B. 8)}$$

where $\boldsymbol{B_0} = [\boldsymbol{N_1'}, \boldsymbol{N_2''}, \boldsymbol{N_3''}, \boldsymbol{N_4'}]^T$ is strain matrix. $\boldsymbol{B_1} = [\boldsymbol{N_2'}, \boldsymbol{N_3'}]^T$. $\boldsymbol{S}$ is the 4×4 matrix of structural properties. $N_1' = \partial \boldsymbol{N_1}/\partial x$ and $N_3'' = \partial^2 \boldsymbol{N_3}/\partial x^2$.

Wind turbine blades are subjected to various applied loads, such as gravitational force, centrifugal force, Coriolis force, aerodynamic loads. Using the principle of virtual work, these applied loads can be generalized as

$$\boldsymbol{F}_{\mathbf{g}}^{\boldsymbol{e}} = \int_0^L \rho_s A \boldsymbol{N}_{\boldsymbol{0}}^{\boldsymbol{T}} dx \cdot \boldsymbol{T}\mathbf{g} \tag{B.9}$$

$$\boldsymbol{F}_{\mathbf{cen}}^{\boldsymbol{e}} = -\int_0^L \rho_s A \boldsymbol{N}_{\boldsymbol{0}}^{\boldsymbol{T}} \boldsymbol{\Omega}\boldsymbol{\Omega} \boldsymbol{N}_{\boldsymbol{0}} (\boldsymbol{x}_{\boldsymbol{e}} + \boldsymbol{q}^{\boldsymbol{e}}) dx = \boldsymbol{F}'_{\boldsymbol{cen}} + \boldsymbol{soft}^{\boldsymbol{e}} \cdot \boldsymbol{q}^{\boldsymbol{e}} \tag{B.10}$$

$$\boldsymbol{F}_{\boldsymbol{cori}}^{\boldsymbol{e}} = -2\int_0^L \rho_s A \boldsymbol{N}_{\boldsymbol{0}}^{\boldsymbol{T}} \boldsymbol{\Omega} \boldsymbol{N}_{\boldsymbol{0}} dx \cdot \dot{\boldsymbol{q}}^{\boldsymbol{e}} = \boldsymbol{cori}^{\boldsymbol{e}} \cdot \dot{\boldsymbol{q}}^{\boldsymbol{e}} \tag{B.11}$$

$$\boldsymbol{F}_{\mathbf{aero}}^{\boldsymbol{e}} = \int_0^L \boldsymbol{N}^{\boldsymbol{T}} \boldsymbol{N}\, \boldsymbol{F}_{\boldsymbol{a}}^{\boldsymbol{e}} dx \tag{B.12}$$

where $\boldsymbol{F}_{\boldsymbol{a}}^{\boldsymbol{e}} = \left[\boldsymbol{F}_{\boldsymbol{x}}^{\boldsymbol{1}},\ \boldsymbol{F}_{\boldsymbol{y}}^{\boldsymbol{1}},\ \boldsymbol{F}_{\boldsymbol{z}}^{\boldsymbol{1}},\ \boldsymbol{M}_{\boldsymbol{x}}^{\boldsymbol{1}},\ \mathbf{0},\ \mathbf{0},\ \boldsymbol{F}_{\boldsymbol{x}}^{\boldsymbol{2}},\ \boldsymbol{F}_{\boldsymbol{y}}^{\boldsymbol{2}},\ \boldsymbol{F}_{\boldsymbol{z}}^{\boldsymbol{2}},\ \boldsymbol{M}_{\boldsymbol{x}}^{\boldsymbol{2}},\ \mathbf{0},\ \mathbf{0}\right]^{\boldsymbol{T}}$ is the elemental nodal aerodynamic loads. $\boldsymbol{soft}^{\boldsymbol{e}}$ and $\boldsymbol{cori}^{\boldsymbol{e}}$ are spin softening matrix and generalized Coriolis matrix, respectively.

Combining the structure related and rotation added terms, the final form of the discretized equation of motion for a rotating blade element is

$$\boldsymbol{M}^{\boldsymbol{e}}\ddot{\boldsymbol{q}}^{\boldsymbol{e}} + (\boldsymbol{C}_{\boldsymbol{0}}^{\boldsymbol{e}} - \boldsymbol{Cori}^{\boldsymbol{e}})\dot{\boldsymbol{q}}^{\boldsymbol{e}} + (\boldsymbol{K}^{\boldsymbol{e}} + \boldsymbol{stress}^{\boldsymbol{e}} - \boldsymbol{soft}^{\boldsymbol{e}})\boldsymbol{q}^{\boldsymbol{e}} = \boldsymbol{F}_{\mathbf{g}}^{\boldsymbol{e}} + \boldsymbol{F}_{\boldsymbol{aero}}^{\boldsymbol{e}} + \boldsymbol{F}'_{\boldsymbol{cen}} \tag{B.13}$$

where $\boldsymbol{C}_{\boldsymbol{0}}^{\boldsymbol{e}}$ is the structural damping matrix.

For the current aero-servo-elastic method, direct usage of partitioned loose-coupling strategy with elastic velocity feedbacks can lead to numerical instabilities, so that a structural damping is adopted to maintain numerical stability where the sectional damping force ($\boldsymbol{F}^{\boldsymbol{Damp}}$) is proportional to the strain rate ($\dot{\boldsymbol{\varepsilon}}$) as

$$\boldsymbol{F}^{\boldsymbol{Damp}} = \mu_i \boldsymbol{S}\dot{\boldsymbol{\varepsilon}} \tag{B.14}$$

The damping forces can be generalized using the principle of virtual work and lead to a stiffness proportional damping matrix for blade beam element as

$$\boldsymbol{C}_{\boldsymbol{0}}^{\boldsymbol{e}} = [\mu]\boldsymbol{K}^{\boldsymbol{e}} \tag{B.15}$$

where $[\mu] = \mathrm{diag}(\mu_1, \mu_2, \mu_3, \mu_4)$ is the diagonal damping coefficient matrix. $\boldsymbol{C}_{\boldsymbol{0}}^{\boldsymbol{e}}$ is the structural damping matrix for a beam element. $\boldsymbol{S}$ is 4×4 sectional stiffness property matrix which is detailed in **Appendix C**.

The damping coefficient μ_i is determined based on the analysis of a single DOF mass-damper-spring system: $m_i\ddot{x} + c_i\dot{x} + k_i x = 0$, of which the circular natural frequency is $\omega_i = 2\pi f_i =$

$\sqrt{k_i/m_i}$ and critical damping is $c_i^0 = 2\sqrt{m_i k_i}$. Therefore, the damping ratio (ξ_i) for a stiffness proportional damping ($c_i = \mu_i k_i$) is

$$\xi_i = \frac{c_i}{c_i^0} = \frac{\mu_i}{2}\sqrt{\frac{m_i}{k_i}} = \frac{1}{2}\mu_i\omega_i = \pi\mu_i f_i \tag{B.16}$$

Eq. (B. 16) reveals the damping coefficient for each degree-of-freedom of a flexible blade can be determined by giving a target damping ratio ξ_i for the target i^{th} mode with natural frequency f_i(HZ), for which the high modes are more damped. In this paper, the damping ratio coefficients of $\mu_i = 1 \times 10^{-3}$ are adopted following the default values in FAST BeamDyn. **Fig. B.1** shows the aeroelastic responses of a NREL 5MW wind turbine at rated conditions (V_0=11.4m/s, Ω = 12.1 rpm, $\theta_p = 0$), wherein the value of $\mu_i = 1 \times 10^{-5}$ leads to case blow up while other values of μ_i predict very similar results.

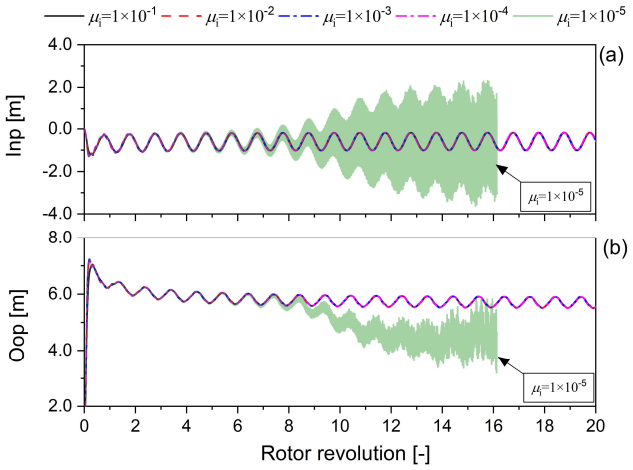

Fig. B.1 Blade tip deflections with different damping ratio coefficients μ_i: (a) In-plane deformations, (b) Out-of-plane deformations.

Appendix C. Bend-Bend coupling

In current method, blade elastic deformations are solved in the blade coordinate system for each blade, while the input sectional stiffness properties, such as flap stiffness and edge stiffness, are defined respective to the sectional principal axis (See **Fig. 2** for the edgewise and flapwise definitions). In sectional coordinate system, the force-deformation relationship has a simple form of

$$\begin{bmatrix} F_{y_p} \\ F_{z_p} \end{bmatrix} = \begin{bmatrix} K_{y_p} & 0 \\ 0 & K_{z_p} \end{bmatrix} \begin{bmatrix} u_{y_p} \\ u_{z_p} \end{bmatrix} \tag{C.1}$$

where K_{y_p} and K_{z_p} are sectional edgewise and flapwise stiffnesses. The $[u_{y_p} \quad u_{z_p}]^T$ and $[F_{y_p} \quad F_{z_p}]^T$ are respective elastic deformation vectors and force vectors in sectional coordinate system.

Eq. (C.1) can be further represented in the blade coordinate system as

$$\boldsymbol{T_1} \begin{bmatrix} F_y \\ F_z \end{bmatrix} = \begin{bmatrix} K_{y_p} & 0 \\ 0 & K_{z_p} \end{bmatrix} \boldsymbol{T_1} \begin{bmatrix} u_y \\ u_z \end{bmatrix} \tag{C.2.a}$$

or equivalently

$$\begin{bmatrix} F_y \\ F_z \end{bmatrix} = \boldsymbol{T_1^T} \begin{bmatrix} K_{y_p} & 0 \\ 0 & K_{z_p} \end{bmatrix} \boldsymbol{T_1} \begin{bmatrix} u_y \\ u_z \end{bmatrix} = \begin{bmatrix} \widetilde{K} \end{bmatrix} \begin{bmatrix} u_y \\ u_z \end{bmatrix} \tag{C.2.b}$$

where $\boldsymbol{T_1}$ is the coordinate transformation matrix as shown in **Eq. (C.3)** and θ is the total angle from rotor plane to sectional chord line, namely, $\theta = \theta_0 + \theta_p - \theta_e$ (See **Fig. 2**).

$$\boldsymbol{T_1} = \begin{bmatrix} \cos(\theta) & \sin(\theta) \\ -\sin(\theta) & \cos(\theta) \end{bmatrix} \tag{C.3}$$

The sectional stiffness property matrix $\begin{bmatrix} \widetilde{K} \end{bmatrix}$ in blade coordinate system is therefore

$$\begin{bmatrix} \widetilde{K} \end{bmatrix} = \begin{bmatrix} K_{yy} & K_{yz} \\ K_{yz} & K_{zz} \end{bmatrix} \tag{C.4}$$

where

$$K_{yy} = K_{yp} \cos^2(\theta) + K_{zp} \sin^2(\theta) \tag{C.5.a}$$

$$K_{zz} = K_{yp}\, sin^2(\theta) + K_{zp}\, cos^2(\theta) \tag{C.5.b}$$

$$K_{yz} = \left(K_{yp} - K_{zp}\right) \sin(\theta) \cos(\theta) \tag{C.5.c}$$

The off-diagonals of $\begin{bmatrix} \widetilde{K} \end{bmatrix}$ are usually non-zero which introduce bend-bend coupling effects unless $K_{yp} = K_{zp}$ or $\theta = 0$. Considering blade elongation and torsion, the total sectional structural stiffness property matrix in blade coordinate system is

$$\boldsymbol{S} = \begin{bmatrix} EA & 0 & 0 & 0 \\ 0 & K_{yy} & K_{yz} & 0 \\ 0 & K_{yz} & K_{zz} & 0 \\ 0 & 0 & 0 & GJ \end{bmatrix} \tag{C.6}$$

The bend-bend coupling effects on blade tip deflections are shown in **Fig. C.1**, wherein the mean in-plane deformation is substantially decreased by 227.8% while the mean out-of-plane deformation is slightly increased by 2.5% for a NREL 5MW wind turbine at rated conditions (V_0=11.4m/s, $\Omega = 12.1$ rpm, $\theta_p = 0°$). Bend-bend coupling effects are essential for accurate predictions of blade in-plane deformation.

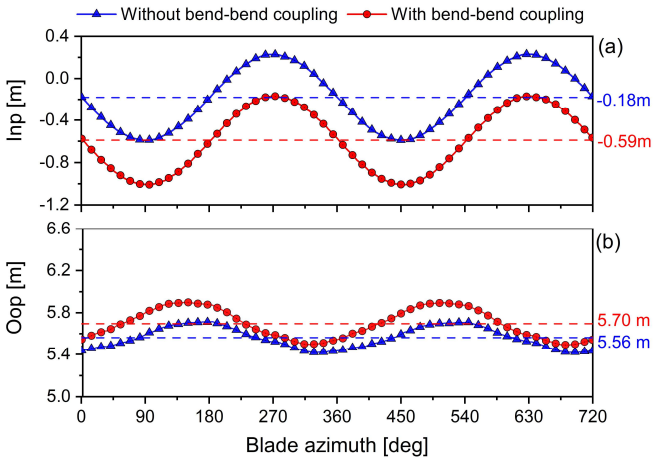

835

836 **Fig. C.1** Bend-bend coupling effects on blade tip deflections: (a) In-plane deformations, (b) Out-of-plane

837 deformations (Dashed lines indicate mean values).

838

Nomenclature

D	Rotor diameter [m]	ρ_a	Air density [kg/m^3]
R	Rotor radius[m]	F_i	Body force term [N/m^3]
r	Blade radial distance[m]	V_0	Streamwise inflow velocity [m/s]
H	Hub height [m]	Ω , Ω_0	Rotor speed, Rated rotor speed [rpm]
N_b	Number of blades	$\bar{c}$	Averaged blade chord
Δ_{min}	Finest grid resolution	c	Chord length [m]
S_0	Global inertial coordinate system	S_t, S_h	Hub, tower coordinate system
S_{b_i}	Blade coordinate system for the i^{th} blade	$S_{c_{i,j}}$	Section coordinate system for the j^{th} section of i^{th} blade
O_0, O_1, O_2	Origin of S_0, S_t, S_h	Θ	Blade azimuth angle [°]
c_0	Root chord of equivalent elliptic wing[m]	c^*	chord of equivalent elliptic wing[m]
F_L,F_D	Lift and Drag forces [N/m]	$\boldsymbol{V}_{rel}$	Sectional relative velocity [m/s]
M_{AC}, M_{PA}	Sectional aerodynamic moments against aerodynamic center and pitch axis position [Nm/m]	$\boldsymbol{V}_{in}$	flow velocity at aerodynamic center[m/s]
$\boldsymbol{V}_{platfrom}$	Sectional velocity due to platform motions [m/s]	$\boldsymbol{V}_{rot}$	Sectional velocity at aerodynamic center due to blade rotation [m/s]
C_L, C_D, C_M	lift, drag and moment coefficients [-]	$\boldsymbol{V}_{elastic}$	Sectional elastic velocity [m/s]
F_T, F_N	Tangential and normal force [N/m]	α	Effective angle of attack [°]
ε	Gaussian smooth length scale [m]	ϕ	Inflow velocity angle [°]
ε^*	Interpolated Gaussian length [m]	θ_0	Initial twist angle [°]
r_s, r_n	Tangential and normal distance [m]	θ_p	Blade pitch angle [°]
Δb	Elemental length [m]	θ_e	Elastic torsional angle [°]
$f_{k,m,i}$	i^{th} component of total aerodynamic force at m^{th} section of k^{th} blade [N/m]	$f^*_{k,i}$	i^{th} component of the interpolated total aerodynamic force from k^{th} blade [N/m]
$\boldsymbol{N_0, N_1, N_2, N_3, N_4}$	Strain matrices	$\boldsymbol{\omega}$	Blade angular velocity vector in S_{b_i}
$\eta_i(x)$	Shape functions	$\omega_x, \omega_y, \omega_z$	x, y, z components of blade angular velocity $\boldsymbol{\omega}$
L	Blade beam element length [m]	$\boldsymbol{\Omega}$	skew symmetric rotational matrix
$\boldsymbol{q^e}$	Beam element displacement	$^{b_i}\boldsymbol{e_x}$, $^{b_i}\boldsymbol{e_y}$,	Vectors in local x, y, z directions of blade coordinate system S_{b_i}
u_x, u_y, u_z	Translational displacements in local x, y, z directions of elastic beam structure [m]	$\mathcal{T}$	Total kinetic energy
$\dot{u}_x, \dot{u}_y, \dot{u}_z$	Translational velocities in local x, y, z directions of elastic beam structure [m/s]	$\mathcal{U}$	Total strain energy
$\theta_x, \theta_y, \theta_z$	Rotational displacements in local x, y, z directions of elastic beam structure [m]	$\mathcal{P}$	Generalized applied load
$\dot{\theta}_x, \dot{\theta}_y, \dot{\theta}_z$	Rotational velocities in local x, y, z directions of elastic beam structure [rad/s]	ρ_s	Mass density of blade section [kg/m^3]
T_x^*	Axial tension force [N]	A	Cross-sectional aero [m^2]
$\boldsymbol{T}$	Coordinate transformation matrix from global to local blade coordinate system.	J	Sectional rotational inertial
$\mathbf{g}$	Gravitational acceleration [m^2/s]	E	Elastic modulus
$\boldsymbol{r}$	Initial radial position	G	Shear modulus
$\boldsymbol{x^e}$	Elastic deformations of beam element	I_y, I_z	sectional moment of inertial relative to local y and z directions
$\boldsymbol{M^e, C_0^e, K^e}$	Elemental mass, damping, and stiffness matrices.	$\boldsymbol{F^e_{aero}}$	Generalized aerodynamic loads.
		$\boldsymbol{F^e_g}$	Generalized gravity loads

$\boldsymbol{stress^e}$	Stress stiffening matrix	$\boldsymbol{F^e_{cen}}$	Generalized centrifugal force
$\boldsymbol{soft^e}$	Spinning softening matrix	$\boldsymbol{F^e_{cori}}$	Generalized Coriolis force
$\boldsymbol{cori^e}$	Coriolis force matrix	$\boldsymbol{F^e_a}$	Elemental aerodynamic loads
$\boldsymbol{S}$	Structural property matrix	$\boldsymbol{M_E, C_E, K_E}$	Assembled mass, damping and stiffness matrices for each blade
$\boldsymbol{B_0, B_1}$	Strain matrices	$\boldsymbol{F_E}$	Assembled generalized loads for each blade
$\widetilde{\Omega}$	Filtered rotor speed	$\Delta\Omega$	Rotor speed error
f_c	Corner frequency for low pass filter	ξ_i	Damping ratio
T_a	Rotor aerodynamic torque [Nm]	$[\mu]$	Damping coefficient matrix
T_{Gen}	Generator torque [Nm]	K_{y_p}, K_{z_p}	Sectional edgewise and flapwise stiffness.
I_D	total drivetrain inertial cast to the LSS	ω	Circular natural frequency [-]
$\dot{\Omega}$	Rotor acceleration	γ	Dimensionless rotor speed
N_{Gear}	Gear box ratio	μ	Dimensionless natural frequency
P_{Gen}, P_{aero}	Generator power and rotor power [W]	X_s	Surge displacement [m]
η	Generator electric efficiency	V_s	Surge velocity [m/s]
K_{P_0}, K_{I_0}	Proportional and integral gains at zero pitch angle	f_s	Surge frequency [HZ]
θ_k	blade pitch angle where the power sensitivity is doubled.	V_c	Normal inflow velocity relative to rotor plane
T_0	Reference rotor thrust [N]	T_x	Rotor thrust in global coordinate system [N]
C_{diss}	Energy dissipation coefficient [-]	W_0	Energy transferred from air flow to surging rotor in one surge period
FOWT	Floating Offshore Wind Turbine	AC	Aerodynamic Center
ACE	Actuator Curve Embedding	PI	Proportional Integral
Inp	In Plane	Oop	Out of Plane
GEBT	Geometrically Exact Beam Theory	FVM	Free Vortex Method
MBD	Multi-Body Dynamic	CSD	Computational Structural Dynamic
FEM	Finite Element Method	FSI	Fluid Structure Interaction
BEM	Blade Element Momentum	ALM	Actuator Line Method
VRS	Vortex Ring State	EALM	Elastic Actuator Line Method
CIP	Constrained Interpolation Profile	LES	Large Eddy Simulation

840

Data Availability

All the data and simulation details in this paper are available on request from the first author. Requests can be sent to: yanglin205@hrbeu.edu.cn. yanglin205@163.com.

Acknowledgments

This work is financially supported by the National Natural Science Foundation of China (grant number: 51739001). The first author acknowledges Dr. J. Jonkman in the National Renewable Energy Laboratory for many useful comments on FAST BeamDyn for definitions and clarifications of the aerodynamic center offset issue for the NREL 5MW wind turbine (See [59, 60]).

Declaration of competing interest

The authors declare that they have no known competing financial interests or personal relationships that could have appeared to influence the work reported in this paper.

References

[1] Global wind report 2021, Global wind energy council,2021,https://gwec.net/global-wind-report-2021/.

[2] J. Jonkman, S. Butterfield, W. Musial, G. Scott, Definition of a 5-MW Reference Wind Turbine for Offshore System Development, National Renewable Energy Laboratory,2009,https://doi.org/10.2172/947422.

[3] E. Gaertner, J.M. Rinker, L. Sethuraman, F. Zahle, B. Anderson, G.E. Barter, N. Abbas, F.Z. Meng, P. Bortolotti, W. Skrzypiński, G.N. Scott, R. Feil, H. Bredmose, K. Dykes, M. Shields, C.K. Allen, A. Viselli, Definition of the IEA 15-Megawatt Offshore Reference Wind Turbine, National Renewable Energy Laboratory (NREL),2020,https://www.nrel.gov/docs/fy20osti/75698.pdf.

[4] H. Namik, K. Stol, Individual blade pitch control of floating offshore wind turbines, Wind Energy 13(1) (2010) 74-85.https://doi.org/10.1002/we.332

[5] K. Ha, H.V.A. Truong, T.D. Dang, K.K. Ahn, Recent Control Technologies for Floating Offshore Wind Energy System: A Review, International Journal of Precision Engineering and Manufacturing-Green Technology 8(1) (2021) 281-301.https://doi.org/10.1007/s40684-020-00269-5

[6] F. Meng, W.H. Lio, A. Pegalajar-Jurado, F. Pierella, E.N. Hofschulte, A.G. Santaya, H. Bredmose, Experimental study of floating wind turbine control on a TetraSub floater with tower velocity feedback gain, Renewable Energy 205 (2023) 509-524.https://doi.org/10.1016/j.renene.2023.01.073

[7] R.J. Barthelmie, K. Hansen, S.T. Frandsen, O. Rathmann, J.G. Schepers, W. Schlez, J. Phillips, K. Rados, A. Zervos, E.S. Politis, P.K. Chaviaropoulos, Modelling and measuring flow and wind turbine wakes in large wind farms offshore, Wind Energy 12(5) (2009) 431-444.https://doi.org/10.1002/we.348

[8] Y. Bazilevs, M.C. Hsu, I. Akkerman, S. Wright, K. Takizawa, B. Henicke, T. Spielman, T.E. Tezduyar, 3D simulation of wind turbine rotors at full scale. Part I: Geometry modeling and aerodynamics, International Journal for Numerical Methods in Fluids 65(1-3) (2011) 207-235.https://doi.org/10.1002/fld.2400

[9] Y. Bazilevs, M.C. Hsu, J. Kiendl, R. Wüchner, K.U. Bletzinger, 3D simulation of wind turbine rotors at full scale. Part II: Fluid–structure interaction modeling with composite blades, International Journal for Numerical Methods in Fluids 65(1-3) (2011) 236-253.https://doi.org/10.1002/fld.2454

[10] C.J. Faccio Júnior, A.C.P. Cardozo, V. Monteiro Júnior, A. Gay Neto, Modeling wind turbine blades by geometrically-exact beam and shell elements: A comparative approach, Engineering Structures 180 (2019) 357-378.https://doi.org/10.1016/j.engstruct.2018.09.032

[11] S. Xu, Y. Xue, W. Zhao, D. Wan, A Review of High-Fidelity Computational Fluid Dynamics for Floating Offshore Wind Turbines, Journal of Marine Science and Engineering 10(10) (2022) 1357.https://doi.org/10.3390/jmse10101357

[12] L. Wang, X. Liu, A. Kolios, State of the art in the aeroelasticity of wind turbine blades: Aeroelastic modelling, Renewable and Sustainable Energy Reviews 64 (2016) 195-210.https://doi.org/10.1016/j.rser.2016.06.007

[13] T.J. Larsen, A.M. Hansen, How 2 HAWC2, the user's manual, Department of Wind Energy,2021,https://tools.windenergy.dtu.dk/HAWC2/manual/How2HAWC2_12_9.pdf.

[14] J. Chen, Z. Hu, G. Liu, D. Wan, Coupled aero-hydro-servo-elastic methods for floating wind turbines, Renewable Energy 130 (2019) 139-153.https://doi.org/10.1016/j.renene.2018.06.060

[15] J.G. Leishman, Principles of Helicopter Aerodynamics, Cambridge University Press, Cambridge,2006.https://www.cambridge.org/gb/academic/subjects/engineering/aerospace-engineering/principles-helicopter-aerodynamics-2nd-edition-1?format=HB&isbn=9781107013353

[16] T. Sebastian, M.A. Lackner, Characterization of the unsteady aerodynamics of offshore floating wind turbines, Wind Energy 16(3) (2013) 339-352.https://doi.org/10.1002/we.545

[17] D.O. Yu, O.J. Kwon, Predicting wind turbine blade loads and aeroelastic response using a coupled CFD–CSD method, Renewable Energy 70 (2014) 184-196.https://doi.org/10.1016/j.renene.2014.03.033

[18] M. Potsdam, H. Yeo, W. Johnson, Rotor Airloads Prediction Using Loose Aerodynamic/Structural

Coupling, Journal of Aircraft 43(3) (2006) 732-742.https://doi.org/10.2514/1.14006
[19] Y. Li, A.M. Castro, T. Sinokrot, W. Prescott, P.M. Carrica, Coupled multi-body dynamics and CFD for wind turbine simulation including explicit wind turbulence, Renewable Energy 76 (2015) 338-361.https://doi.org/10.1016/j.renene.2014.11.014
[20] Y. Liu, Q. Xiao, A. Incecik, C. Peyrard, Aeroelastic analysis of a floating offshore wind turbine in platform-induced surge motion using a fully coupled CFD-MBD method, Wind Energy 22(1) (2019) 1-20.https://doi.org/10.1002/we.2265
[21] G. Guma, G. Bangga, T. Lutz, E. Krämer, Aeroelastic analysis of wind turbines under turbulent inflow conditions, Wind Energ. Sci. 6(1) (2021) 93-110.https://doi.org/10.5194/wes-6-93-2021
[22] J.C. Heinz, N.N. Sørensen, F. Zahle, Fluid–structure interaction computations for geometrically resolved rotor simulations using CFD, Wind Energy 19(12) (2016) 2205-2221.https://doi.org/10.1002/we.1976
[23] C. Grinderslev, N.N. Sørensen, S.G. Horcas, N. Troldborg, F. Zahle, Wind turbines in atmospheric flow: fluid–structure interaction simulations with hybrid turbulence modeling, Wind Energ. Sci. 6(3) (2021) 627-643.https://doi.org/10.5194/wes-6-627-2021
[24] B. Dose, H. Rahimi, I. Herráez, B. Stoevesandt, J. Peinke, Fluid-structure coupled computations of the NREL 5 MW wind turbine by means of CFD, Renewable Energy 129 (2018) 591-605.https://doi.org/10.1016/j.renene.2018.05.064
[25] A. Alkhabbaz, H.-S. Yang, W. Tongphong, Y.-H. Lee, Impact of compact diffuser shroud on wind turbine aerodynamic performance: CFD and experimental investigations, International Journal of Mechanical Sciences 216 (2022) 106978.https://doi.org/10.1016/j.ijmecsci.2021.106978
[26] A. Alkhabbaz, H.-S. Yang, A.H.S. Weerakoon, Y.-H. Lee, A novel linearization approach of chord and twist angle distribution for 10 kW horizontal axis wind turbine, Renewable Energy 178 (2021) 1398-1420.https://doi.org/10.1016/j.renene.2021.06.077
[27] J.N. Sørensen, W.Z. Shen, Numerical Modeling of Wind Turbine Wakes, Journal of Fluids Engineering-transactions of The Asme 124(2) (2002) 393-399.https://doi.org/10.1115/1.1471361
[28] H. Meng, F.-S. Lien, L. Li, Elastic actuator line modelling for wake-induced fatigue analysis of horizontal axis wind turbine blade, Renewable Energy 116 (2018) 423-437.https://doi.org/10.1016/j.renene.2017.08.074
[29] H. Meng, L. Li, J. Zhang, A preliminary numerical study of the wake effects on the fatigue load for wind farm based on elastic actuator line model, Renewable Energy 162 (2020) 788-801.https://doi.org/10.1016/j.renene.2020.07.140
[30] Z. Ma, P. Zeng, L. Lei, Analysis of the coupled aeroelastic wake behavior of wind turbine, Journal of Fluids and Structures 84 (2019) 466-484.https://doi.org/10.1016/j.jfluidstructs.2018.09.001
[31] G. Della Posta, S. Leonardi, M. Bernardini, Large eddy simulations of a utility-scale horizontal axis wind turbine including unsteady aerodynamics and fluid-structure interaction modelling, Wind Energy 26(1) (2023) 98-125.https://doi.org/10.1002/we.2789
[32] J. Leng, Z. Gao, M.C.H. Wu, T. Guo, Y. Li, A fluid–structure interaction model for large wind turbines based on flexible multibody dynamics and actuator line method, Journal of Fluids and Structures 118 (2023) 103857.https://doi.org/10.1016/j.jfluidstructs.2023.103857
[33] J. Zheng, N. Wang, D. Wan, S. Strijhak, Numerical investigations of coupled aeroelastic performance of wind turbines by elastic actuator line model, Applied Energy 330 (2023) 120361.https://doi.org/10.1016/j.apenergy.2022.120361
[34] B. Elie, G. Oger, L. Vittoz, D. Le Touzé, Simulation of two in-line wind turbines using an incompressible Finite Volume solver coupled with a Blade Element Model, Renewable Energy 187 (2022) 81-93.https://doi.org/10.1016/j.renene.2021.12.082
[35] Z. Yu, Q. Ma, X. Zheng, K. Liao, H. Sun, A. Khayyer, A hybrid numerical model for simulating aero-elastic-hydro-mooring-wake dynamic responses of floating offshore wind turbine, Ocean Engineering 268 (2023) 113050.https://doi.org/10.1016/j.oceaneng.2022.113050
[36] L. Yang, K. Liao, Q. Ma, G. Ma, H. Sun, Investigation of wake characteristics of floating offshore wind turbine with control strategy using actuator curve embedding method, Renewable Energy 218 (2023) 119255.https://doi.org/10.1016/j.renene.2023.119255
[37] P.K. Jha, S. Schmitz, Actuator curve embedding – an advanced actuator line model, Journal of Fluid Mechanics 834 (2018) R2.https://doi.org/10.1017/jfm.2017.793
[38] F. Xiao, T. Yabe, Completely Conservative and Oscillationless Semi-Lagrangian Schemes for Advection Transportation, Journal of Computational Physics 170(2) (2001) 498-

522.https://doi.org/10.1006/jcph.2001.6746
[39] C. Hu, M. Kashiwagi, A CIP-based method for numerical simulations of violent free-surface flows, Journal of Marine Science and Technology 9(4) (2004) 143-157.https://doi.org/10.1007/s00773-004-0180-z
[40] S.N. Rodriguez, J.W. Jaworski, Strongly-coupled aeroelastic free-vortex wake framework for floating offshore wind turbine rotors. Part 1: Numerical framework, Renewable Energy 141 (2019) 1127-1145.https://doi.org/10.1016/j.renene.2019.04.019
[41] Z. Li, B. Wen, X. Dong, Z. Peng, Y. Qu, W. Zhang, Aerodynamic and aeroelastic characteristics of flexible wind turbine blades under periodic unsteady inflows, Journal of Wind Engineering and Industrial Aerodynamics 197 (2020) 104057.https://doi.org/10.1016/j.jweia.2019.104057
[42] G. Della Posta, S. Leonardi, M. Bernardini, A two-way coupling method for the study of aeroelastic effects in large wind turbines, Renewable Energy 190 (2022) 971-992.https://doi.org/10.1016/j.renene.2022.03.158
[43] X. Zhu, J. Chen, X. Shen, Z. Du, Impact of Blade Flexibility on Wind Turbine Loads and Pitch Settings, Journal of Solar Energy Engineering 141(4) (2019).https://doi.org/10.1115/1.4042315
[44] K. Vimalakan, NREL 5MW Rotor Geometry, 2011. https://forums.nrel.gov/t/nrel-5mw-rotor-geometry/330. (Accessed 18th November 2023).
[45] P.K. Jha, M.J. Churchfield, P. Moriarty, S. Schmitz, Guidelines for Volume Force Distributions Within Actuator Line Modeling of Wind Turbines on Large-Eddy Simulation-Type Grids, Journal of Solar Energy Engineering-transactions of The Asme 136(3) (2014) 031003.https://doi.org/10.1115/1.4026252
[46] J.J. Q. Wang, M. Sprague, and B. Jonkman, BeamDyn User's Guide and Theory Manual, 2016,https://www.nrel.gov/wind/nwtc/assets/downloads/BeamDyn/BeamDyn_Manual.pdf.
[47] M.-S. Jeong, M.-C. Cha, S.-W. Kim, I. Lee, T. Kim, Effects of torsional degree of freedom, geometric nonlinearity, and gravity on aeroelastic behavior of large-scale horizontal axis wind turbine blades under varying wind speed conditions, Journal of Renewable and Sustainable Energy 6(2) (2014) 023126.https://doi.org/10.1063/1.4873130
[48] C.G. Gebhardt, B.A. Roccia, Non-linear aeroelasticity: An approach to compute the response of three-blade large-scale horizontal-axis wind turbines, Renewable Energy 66 (2014) 495-514.https://doi.org/10.1016/j.renene.2013.12.040
[49] A.D. Wright, C.E. Smith, R.W. Thresher, J.L.C. Wang, Vibration Modes of Centrifugally Stiffened Beams, Journal of Applied Mechanics 49(1) (1982) 197-202.https://doi.org/10.1115/1.3161966
[50] M. Imiela, F. Wienke, Towards Multidisciplinary Wind Turbine Design using High-Fidelity Methods, 33rd Wind Energy Symposium, American Institute of Aeronautics and Astronautics, 2015.https://doi.org/10.2514/6.2015-1462
[51] F.L. Ponta, A.D. Otero, L.I. Lago, A. Rajan, Effects of rotor deformation in wind-turbine performance: The Dynamic Rotor Deformation Blade Element Momentum model (DRD–BEM), Renewable Energy 92 (2016) 157-170.https://doi.org/10.1016/j.renene.2016.01.098
[52] A. Sabale, K.V.N. Gopal, Nonlinear aeroelastic response of wind turbines using Simo-Vu-Quoc rods, Applied Mathematical Modelling 65 (2019) 696-716.https://doi.org/10.1016/j.apm.2018.09.003
[53] A.K. Sabale, N.K.V. Gopal, Nonlinear Aeroelastic Analysis of Large Wind Turbines Under Turbulent Wind Conditions, AIAA Journal 57(10) (2019) 4416-4432.https://doi.org/10.2514/1.J057404
[54] C. Lienard, R. Boisard, C. Daudin, Aerodynamic Behavior of a Floating Offshore Wind Turbine, AIAA Journal 58(9) (2020) 3835-3847.https://doi.org/10.2514/1.J059255
[55] J. Jonkman, Influence of Control on the Pitch Damping of a Floating Wind Turbine, 46th AIAA Aerospace Sciences Meeting and Exhibit, American Institute of Aeronautics and Astronautics, 2008.https://doi:10.2514/6.2008-1306
[56] D.D. Apsley, P.K. Stansby, Unsteady thrust on an oscillating wind turbine: Comparison of blade-element momentum theory with actuator-line CFD, Journal of Fluids and Structures 98 (2020) 103141.https://doi.org/10.1016/j.jfluidstructs.2020.103141
[57] J.C.R. Hunt, A. Wray, P. Moin, Eddies, stream, and convergence zones in turbulent flows, Studying Turbulence Using Numerical Simulation Databases, 2. Proceedings of the 1988 Summer Program, 1988, pp. 193-208.https://ntrs.nasa.gov/api/citations/19890015184/downloads/19890015184.pdf

[58] J. Jeong, F. Hussain, On the identification of a vortex, Journal of Fluid Mechanics 285 (1995) 69-94.https://doi.org/10.1017/S0022112095000462
[59] L. Yang, Aerodynamic center offset effects on blade torsion, 2023. https://forums.nrel.gov/t/aerodynamic-center-offset-effects-on-blade-torsion/4841/2. (Accessed April 19th 2023).
[60] L. Yang, Comparing ElastoDyn with BeamDyn for blade tip deformations, 2023. https://forums.nrel.gov/t/comparing-elastodyn-with-beamdyn-for-blade-tip-deformations/4774. (Accessed April 4th 2023).